

**1 A theory for how the depth of meltwater injection impacts regional sea level
2 evolution**

3 Aurora Basinski-Ferris^a, Laure Zanna^a, and Ian Eisenman^b

4 ^a Courant Institute of Mathematical Sciences, New York University, New York, NY, USA

5 ^b Scripps Institution of Oceanography, University of California San Diego, La Jolla, CA, USA

6 Corresponding author: Aurora Basinski-Ferris, abf376@nyu.edu

7 ABSTRACT: Mass loss from the Antarctic ice sheet is projected to continue over the coming
8 century. The resultant sea level change will have a regional pattern that evolves over time as the
9 ocean adjusts. Accurate estimation of this evolution is crucial for local communities. Current
10 state-of-the-art climate models typically do not couple ice sheets to the atmosphere-ocean system,
11 and the impact of ice sheet melt has often been studied by injecting meltwater at the model ocean
12 surface. However, observational evidence suggests that most Antarctic meltwater enters the ocean
13 at depth through ice shelf basal melt. A previous study has demonstrated that the regional sea level
14 pattern at a given time depends on meltwater injection depth. Here, we introduce a 2.5-layer model
15 to investigate this dependence and develop a theory for the associated adjustment mechanisms. We
16 find mechanisms consistent with previous literature on the ocean adjustment to changes in forcing,
17 whereby a slower Rossby wave response off the eastern boundary follows a fast response from the
18 western boundary current and Kelvin waves. We demonstrate that faster baroclinic Rossby waves
19 near the surface than at depth explains the injection depth dependence of the adjustment in the
20 2.5-layer model. The identified Rossby wave mechanism may contribute to the dependence of the
21 ocean's transient adjustment on meltwater injection depth in more complex models. This work
22 highlights processes that could cause errors in the projection of the time-varying pattern of sea
23 level rise using surface meltwater input to represent Antarctica's freshwater forcing.

24 SIGNIFICANCE STATEMENT: Sea level rise is expected to be larger in some locations than
25 others. Accurate projections of the pattern of sea level change, which changes in time as the ocean
26 adjusts, is essential information for local communities. One of the factors that leads to uncertainty
27 in the local sea level change due to Antarctic melt is the depth at which this meltwater is input into
28 an ocean model. We propose a mechanism for a faster response of sea level around the basin when
29 meltwater is injected at the ocean surface compared to when it is injected well below the surface.
30 This mechanism has implications for projections of the regional sea level response to Antarctic
31 melt.

32 1. Introduction

33 During recent decades, Antarctica has been losing mass, which has caused a global mean sea
34 level increase from 1992 to 2020 of 7.4 ± 1.5 millimeters (Otosaka et al. 2023). Projections indicate
35 continued Antarctic mass loss, likely raising global mean sea level by up to 28cm by 2100 and
36 driving an accelerated rise into the 22nd century (Oppenheimer et al. 2019). In particular, West
37 Antarctica, which is the location of the most mass loss on the Antarctic ice sheet (Adusumilli et al.
38 2020), has a capacity to raise global mean sea level by 5.3m if the ice completely melts (Morlighem
39 et al. 2020, Table S3). However, contributions to sea level rise, such as from ice sheets, glaciers, and
40 steric changes, are not globally uniform (e.g., Kopp et al. 2015; Hamlington et al. 2020; Todd et al.
41 2020). For adaptation efforts, projecting the time-evolving pattern of regional sea level change is
42 particularly crucial. In the case of sea level rise from ice sheet melt, regional variation in sea level
43 will be determined by changes in Earth's gravitation, rotation, and deformation (e.g., Farrell and
44 Clark 1976; Kopp et al. 2010; Mitrovica et al. 2018), as well as ocean dynamic processes which
45 propagate and are affected by the meltwater injection (e.g., Stammer 2008; Lorbacher et al. 2012;
46 Kopp et al. 2010; Schmidt et al. 2023).

47 The largest contributor to Antarctic mass loss is the basal melt of ice shelves (Pritchard et al.
48 2012; Rignot et al. 2013; Depoorter et al. 2013). Observations near west Antarctic ice shelves
49 indicate that this meltwater settles at depth after exiting the ice shelf cavity (Kim et al. 2016;
50 Garabato et al. 2017), likely due to turbulent mixing processes between the meltwater plume and
51 the rest of the water column (Garabato et al. 2017). However, full complexity atmosphere-ocean
52 models, including those in the CMIP5 and CMIP6 ensembles, are not currently coupled to ice

sheet models (Taylor et al. 2012; Eyring et al. 2016), although there has been recent work in this direction (Smith et al. 2021). Thus, climate projections with meltwater forcing included are typically performed by prescribing a freshwater input, which is often added to the surface net precipitation field, known as “hosing experiments” (e.g., Stammer 2008; Lorbacher et al. 2012; Kopp et al. 2010; Bronselaer et al. 2018; Golledge et al. 2019; Moorman et al. 2020; Li et al. 2023b; Schmidt et al. 2023; Park et al. 2023). This discrepancy between the vertical distribution of meltwater in observations and the typical approach in modelling studies motivated a previous study which demonstrated in a simplified single basin model that an idealized representation of Antarctic meltwater injected at depth adjusts the dynamic sea level more slowly across the basin than meltwater injected at the surface (Eisenman et al. 2024). This sensitivity to vertical meltwater distribution falls under a broad category of potential sensitivities of the ocean response to choices in meltwater hosing experiments, which have been identified as targets for community investigation (Swart et al. 2023).

Here, we focus on the baroclinic response of sea level to meltwater input, which largely determines the dynamic sea level pattern, and occurs after a spatially uniform and rapid barotropic response (Eisenman et al. 2024). We present a simplified model and develop a theory to explore the difference in this baroclinic adjustment when inputting a volume anomaly at depth compared to at the surface, which ultimately leads to a different sea level pattern at a given time. We utilize a reduced gravity model, which is a class of models that is used for simplified representations of the upper ocean. For example, reduced gravity models have been utilized in simple models of El Niño (e.g., Cane and Zebiak 1985; Chang et al. 2006; Guo et al. 2022) and to understand adjustment to changes in deep water formation (e.g., Kawase 1987; Huang et al. 2000; Johnson and Marshall 2002, 2004; Cessi et al. 2004; Zhai et al. 2011; Nieves and Spall 2018; Sun et al. 2020), North Atlantic or Southern Ocean heat sources (Hsieh and Bryan 1996), and changes in wind stress (e.g., Cessi and Othegeuy 2003; Zhai et al. 2014). In the present work, we examine the large scale dynamical adjustment to volume input at the southern end of a rectangular domain utilizing a reduced gravity model with two active layers (2.5-layer model). Much of the theory developed is analogous to previous studies of other phenomena (e.g., Johnson and Marshall 2002), but we include an additional active layer, to investigate the vertical dependence of the adjustment processes.

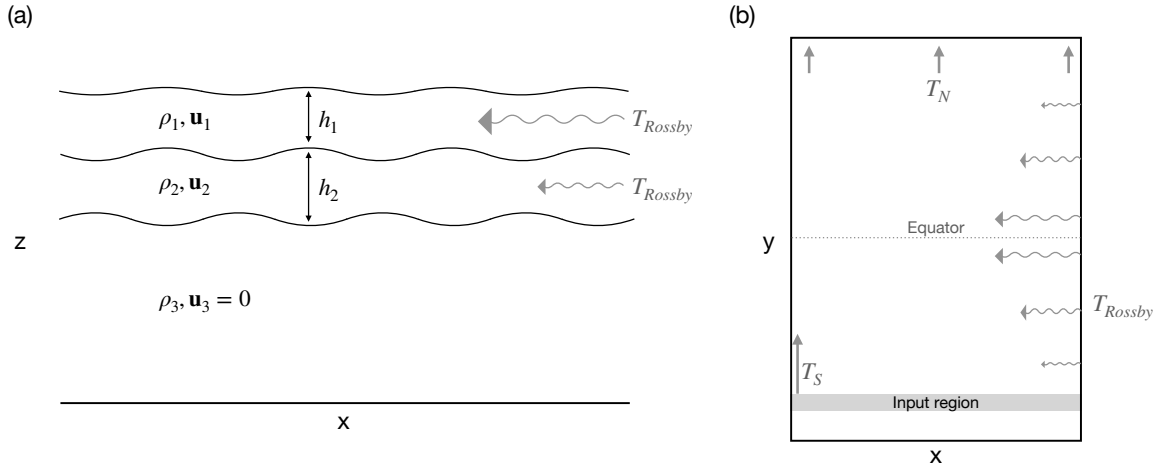


FIG. 1. Adjustment mechanism schematic in 2.5-layer reduced gravity model. (a) model set-up in longitude and depth space. The top two layers are active with unconstrained \mathbf{u}_i , while the abyssal (third) layer is motionless. We highlight the essential mechanism of adjustment (see Section 3), whereby a top-layer volume perturbation propagates an upper ocean anomaly faster than a bottom-layer perturbation due to faster baroclinic Rossby waves. (b) the domain in longitude and latitude space with a schematic of the adjustment mechanism. In both panels, the notation T_{Rossby} is used as in Johnson and Marshall (2002) and indicates volume fluxes due to Rossby waves.

This paper is organized as follows: in Section 2, we introduce the 2.5-layer model and compare this idealized model to the results in Eisenman et al. (2024). We present an analytic theory for the ocean's dynamical response to meltwater input in Section 3, highlighting the essential physical processes that lead to faster transport of a meltwater perturbation near the surface compared to at depth. In Section 4, we discuss the sensitivity of the results to parameter choices and the potential effect of Ekman transport. We conclude in Section 5.

2. Dynamic adjustment to meltwater input in a hierarchy of numerical simulations

As presented in Eisenman et al. (2024) using runs in MITgcm, the adjustment of dynamic sea level throughout a single basin is slower for idealized Antarctic meltwater perturbations injected

at depth than for perturbations injected at the surface. In particular, this difference in adjustment
 was attributed to the different timescales associated with the baroclinic (largely steric) response
 of the ocean (following rapid barotropic waves, which have a largely globally uniform imprint).
 Here, we introduce a simplified model, designed to capture baroclinic processes, to investigate the
 adjustment mechanisms and the difference in propagation of anomalies input at depth compared to
 at the surface.

a. 2.5-layer model set-up

We define a 2.5-layer reduced gravity model consisting of 2 active layers with densities ρ_1 and
 ρ_2 on top of a quiescent abyss with density ρ_3 . The abyss is a layer of no motion and, thus, has
 horizontally uniform pressure. The model is defined with linearized momentum equations and
 non-linear continuity equations:

$$\frac{\partial \mathbf{u}_i}{\partial t} + \mathbf{f} \times \mathbf{u}_i = -\delta_{i,1} g'_1 \nabla h_1 - g'_2 \nabla(h_1 + h_2) + \nu \nabla^2 \mathbf{u}_i - r \mathbf{u}_i, \quad (1)$$

$$\frac{D h_i}{D t} + h_i \nabla \cdot \mathbf{u}_i = S_i(x, y), \quad (2)$$

where $\delta_{i,1}$ is a Kronecker delta. Here, h_i is the layer thickness in the i^{th} layer with $i = 1, 2$,
 $\mathbf{u}_i = (u_i, v_i)$ is the velocity vector, ∇ is the two-dimensional gradient operator, $g'_i = g^{\frac{\rho_{i+1}-\rho_i}{\rho_0}}$ is the
 i^{th} reduced gravity with ρ_0 the reference density, $\frac{D}{D t} = \left(\frac{\partial}{\partial t} + \mathbf{u} \cdot \nabla \right)$ is the material derivative, and
 ν is the viscosity coefficient set to $\nu = 8 \times 10^3 \text{ m}^2 \text{s}^{-1}$. The Rayleigh friction term is only active in
 the sponge layers (see Figure 2) which are described in detail in Appendix A. Imposed sources and
 sinks in the domain in layer i are denoted as $S_i(x, y)$, while initial layer thicknesses prior to the
 introduction of sources or sinks will be denoted H_i . A schematic of the model is shown in Figure
 1a. The domain size is chosen to have the same surface area as that of the MITgcm set-up that we
 compare against; however, the domains have different shapes because the 2.5-layer model is run
 in a rectangular domain on a Cartesian grid, whereas MITgcm is run on a latitude-longitude grid.
 Details for the numerical solution of the 2.5-layer model are given in Appendix A.

119 We test the sensitivity of adjustment mechanisms to a zonal wind forcing in the southern part of
120 the domain in the 2.5-layer model simulations by modifying Equation (1) such that:

$$\frac{\partial \mathbf{u}_i}{\partial t} + \mathbf{f} \times \mathbf{u}_i = -\delta_{i,1} g'_1 \nabla h_1 - g'_2 \nabla(h_1 + h_2) + v \nabla^2 \mathbf{u}_i - r \mathbf{u}_i + \delta_{i,1} \frac{\boldsymbol{\tau}}{\rho_1 H_1}, \quad (3)$$

121 where $\boldsymbol{\tau} = (\tau(y, t), 0)$ is the imposed zonal wind forcing.

122 In this work, we focus on two types of perturbation experiments, designed as simplified representations of Antarctic meltwater input at different depths (see Figure 2): volume additions into
123 (1) the top active layer ($i = 1$) and (2) the bottom active layer ($i = 2$).
124

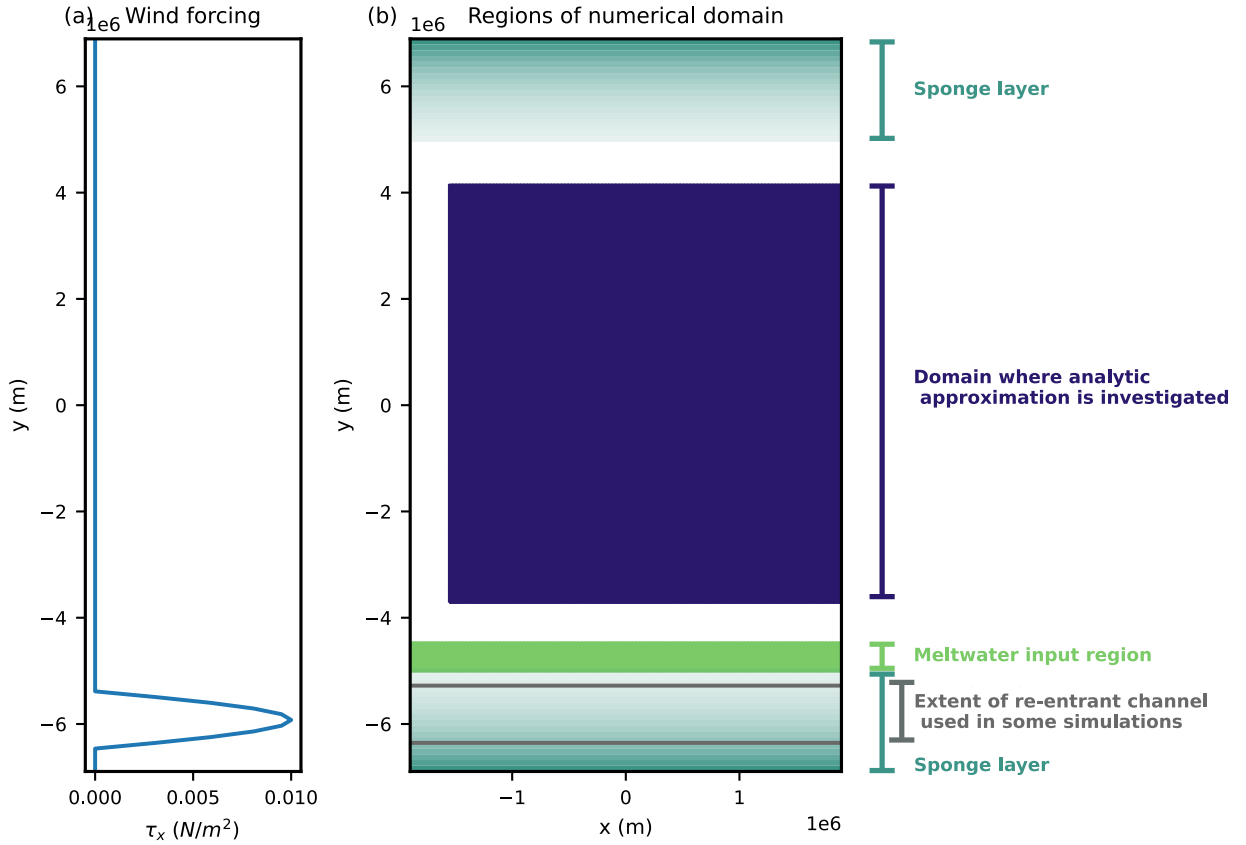
135 b. *Upper ocean response in MITgcm and the 2.5-layer model*

136 In a Boussinesq ocean model, such as MITgcm, the free surface evolves due to volume convergence which may occur due to transport processes at any depth. Here, we focus on the upper ocean
137 thickness, which is reflective of the transport in the upper ocean. We determine the upper ocean
138 thickness, $h_u(x, y, t)$, as the thickness above a given isopycnal that correlates to the upper ocean in
139 the control state (located at approximately 1000m depth, see Figure B1):
140

$$h_u(x, y, t) = \sum_1^n h_i(x, y, t), \quad (4)$$

141 where h_i is the thickness associated with the i th isopycnal layer and n is the layer chosen to sum
142 up to; here, potential density increases with increasing layer number. The h_i layers adjust due to
143 convergence of volume within the layers (in a Boussinesq model, this includes mixing processes).
144 In the 2.5-layer model presented in this paper, a comparable metric of the upper ocean thickness is
145 the sum of the thickness of the active layers ($h_1 + h_2$), which are representing the upper ocean.

146 In Figure 3, we focus on this upper ocean thickness metric in both models. In particular,
147 we examine the Northern Hemisphere upper ocean thickness anomaly, which is the Northern
148 Hemisphere mean upper ocean thickness minus the global mean upper ocean thickness. We
149 focus on the Northern Hemisphere anomaly, as this is indicative of the response at the *opposite*
150 end of the basin from the meltwater input, and thus summarizes the adjustment throughout the
151 basin. Comparable plots would be equal and opposite for the Southern Hemisphere anomaly, when
152 averaging over the whole domain (i.e., not just the analytic region).



125 FIG. 2. (a): Wind forcing profile; (b) Diagram showing domain regions used for the 2.5-layer reduced gravity
 126 model. The extent of the sponge layers is defined as regions where *any* Rayleigh damping is present. Note that
 127 the strength of the damping decays exponentially away from the north/south walls, as illustrated in the diagram,
 128 although the visual representation of this decay is less strong than in the numerical solution. In purple, we denote
 129 the region where we solve for the theoretical solution in Section 3 (analytic domain); the meltwater input region
 130 (green) is at the southern edge of the analytic domain. The analytic region excludes the western boundary current
 131 region and a few grid cells near the sponge layers in order to focus on: (1) the dynamics in the interior, and (2)
 132 the region unaffected by numerical effects from the sponge layers. The re-entrant channel region is shown, but it
 133 is only utilized in experiments where wind is applied. Note that the re-entrant channel is within the sponge layer,
 134 but is located where the damping is sufficiently weak to allow Ekman transport to be driven.

153 Figure 3a shows the Northern Hemisphere upper ocean thickness anomaly, scaled by the total
 154 thickness change around the first equilibration of the deep perturbation (at year 110 after meltwater
 155 introduction) in the simulations presented in Eisenman et al. (2024). The faster adjustment of

156 Northern Hemisphere sea level in experiments with meltwater anomalies input at the surface
157 compared to anomalies input at depth is driven by the upper ocean thickness, as we capture the
158 faster adjustment in this metric. Thus, the upper ocean processes are key to explaining the result in
159 Eisenman et al. (2024), which demonstrated faster propagation of steric anomalies away from the
160 input region in a surface perturbation experiment compared to a deep perturbation experiment.

161 Figure 3b and c presents results for the adjustment of volume perturbations in the 2.5-layer model,
162 which are introduced when the ocean is at rest such that the meltwater perturbation itself induces
163 all transport. We choose $g'_1 = g'_2 = g \frac{2}{1026}$ and initial layer thicknesses $H_1 = H_2 = 250\text{m}$ as physically
164 reasonable upper ocean parameter choices (see Section 4a for the sensitivity to parameters). We
165 input a volume perturbation via a step function of 0.1 Sv into the input region of either layer 1 or 2,
166 as indicated in Figure 2b. Figure 3b shows the Northern Hemisphere upper ocean scaled thickness
167 anomaly, which is normalized by the equilibrated total thickness anomaly (year 41 after meltwater
168 input), such that this quantity is directly comparable to Figure 3a. As in MITgcm, we find that
169 the upper ocean thickness adjusts more quickly in the Northern Hemisphere due to a top-layer
170 perturbation than a bottom-layer perturbation (Figure 3b). We include an analytic estimate (dashed
171 lines), developed in Section 3, by taking the Northern Hemisphere mean over the purple region
172 in Figure 2; see Appendix A for a small quantitative difference in the numerical result averaged
173 over the entire domain. In Figure 3a and b, we have scaled by the global mean change for the best
174 comparison between models because the global mean upper ocean thickness changes entirely due
175 to meltwater input in the 2.5-layer model, but is larger in the MITgcm simulations because mixing
176 processes also affect the volume. Figure 3c is comparable to Figure 3b, but without scaling by the
177 global mean thickness change.

178 The 2.5-layer model has a small sea level change which is not equivalent to the upper ocean
179 thickness metric chosen here (see Appendix B2). However, we find that the initial result presented
180 in Eisenman et al. (2024), which demonstrated faster adjustment of dynamic sea level throughout
181 the basin in a surface perturbation experiment compared to a deep perturbation experiment, is
182 driven by the adjustment of the upper ocean. Thus, we focus on this upper ocean adjustment, and
183 we develop a theory which can explain key mechanisms and their associated relative timescales in
184 the simplified model.

199 **3. An analytical theory for adjustment**

200 We aim to develop an analytical theory for the dynamical response to volume input near the
201 southern edge of the 2.5-layer model. We assume that adjustment mechanisms similar to other
202 reduced gravity model studies will prevail (e.g., Kawase 1987; Hsieh and Bryan 1996; Huang et al.
203 2000; Johnson and Marshall 2002, 2004; Cessi et al. 2004; Zhai et al. 2011; Nieves and Spall
204 2018), but we consider the processes with an additional active layer compared to these previous
205 studies. That is, we assume that the height perturbation is first propagated by a fast response such
206 that: (1) the volume anomaly induces a transport along the western boundary, which propagates
207 some volume northward, toward the equator; (2) the volume anomaly travels across the equator
208 as a Kelvin wave; (3) the volume anomaly travels along the eastern boundary as Kelvin waves,
209 resulting in near uniform height along the boundary. The height anomaly's slower propagation
210 into the basin's interior is then governed by baroclinic Rossby waves emanating from the eastern
211 boundary. As we are interested in the multidecadal to centennial adjustment, we view the three
212 fast mechanisms above as occurring instantaneously, and we aim to develop an analytic theory to
213 explain the relatively slow adjustment driven by the propagation of baroclinic Rossby waves. In
214 particular, we aim for the theory developed to highlight the vertical dependence of the processes
215 which adjust the upper ocean thickness anomaly throughout the basin (here indicated by the
216 Northern Hemisphere anomaly, see Figure 3).

217 *a. Assumptions and preliminaries*

218 We approximate that the relevant dynamics for volume adjustment in the interior of the basin on
219 multidecadal to centennial timescales are captured by geostrophic balance

$$f\mathbf{u}_i = \mathbf{k} \times \nabla (g'_2(h_1 + h_2) + \delta_{i,1}g'_1h_1), \quad (5)$$

220 and the continuity equations linearized around the starting layer thicknesses (H_i) with no source or
221 sink terms

$$\frac{\partial h_i}{\partial t} + H_i \nabla \cdot \mathbf{u}_i = 0, \quad (6)$$

222 for layers $i = 1, 2$. In Equation (5), the Rayleigh damping term is absent, since it is only active
223 in the sponge layers. We have, however, assumed that the viscous term can be neglected in the

224 interior (although it is an important term in the western boundary current region to close the
 225 basin's circulation). We obtain evolution equations for the interior layer thicknesses by combining
 226 Equations (5) and (6):

$$\frac{\partial h_i}{\partial t} + \frac{H_i \beta g'_2}{f^2} \frac{\partial(h_1 + h_2)}{\partial x} + \delta_{i,1} \frac{H_1 \beta g'_1}{f^2} \frac{\partial h_1}{\partial x} = 0, \quad (7)$$

227 with $i = 1, 2$ and $\beta \equiv \frac{df}{dy}|_\theta$ evaluated at a given latitude θ . Here, we will utilize a beta plane
 228 approximation centered at the equator, and thus $\beta \approx 2.20 \times 10^{-11} \text{ m}^{-1} \text{s}^{-1}$. The advection equa-
 229 tions (Equation 7) differ between the two active layers of the model due to the representation of
 230 geostrophic balance, which includes an additional term in the top-layer ($i = 1$). This layer-wise
 231 difference in the geostrophic velocities corresponds to the model's thermal wind relation.

232 b. Rossby wave adjustment off the eastern boundary

233 To capture the multidecadal adjustment, we proceed by solving Equation (7). For simplicity, we
 234 use that $H \equiv H_1 = H_2$ and $g'_1 = g'_2$ and denote $c(y) = \frac{\beta g'_2}{f^2} = \frac{\beta g'_1}{f^2}$. (In Appendix D1, we relax these
 235 assumptions and present a general solution). We rewrite the coupled advection system given by
 236 Equation (7) for both layers as:

$$\frac{\partial \mathbf{h}}{\partial t} + \mathbf{A} \cdot \frac{\partial \mathbf{h}}{\partial x} = 0, \quad (8)$$

237 with $\mathbf{h}(x, y, t) = [h_1(x, y, t), h_2(x, y, t)]$ and

$$\mathbf{A} = H c(y) \begin{bmatrix} 2 & 1 \\ 1 & 1 \end{bmatrix}. \quad (9)$$

238 We diagonalize the matrix $\mathbf{A} = \mathbf{P}^{-1} \Lambda \mathbf{P}$ to decouple the equations in a new set of variables $\mathbf{w}(x, y, t) =$
 239 $[w_1, w_2] = \mathbf{P} \mathbf{h}$. The decoupled linear advection equations in the variable \mathbf{w} are given by

$$\frac{\partial \mathbf{w}}{\partial t} + \Lambda \frac{\partial \mathbf{w}}{\partial x} = 0, \quad (10)$$

where the entries of $\Lambda = (\lambda_1, \lambda_2)$ are the eigenvalues of \mathbf{A} , $\lambda_1(y) = \frac{3+\sqrt{5}}{2}Hc(y)$ and $\lambda_2(y) = \frac{3-\sqrt{5}}{2}Hc(y)$. The solution for each variable is given using the method of characteristics such that

$$w_i(x, y, t) = w_i(x - \lambda_i(y)t, y, 0), \quad (11)$$

for $i = 1, 2$. Equation (11) indicates that information shifts (westward) at the speed given by the eigenvalue. Given our hypothesized mechanism, which has the eastern boundary approximately equilibrated through the fast response, we interpret Equation (11) as a set of delay equations off the eastern boundary. We perform a transformation back to \mathbf{h} coordinates and write the variables explicitly in terms of the eastern boundary timeseries:

$$h_1(x, y, t) = \underbrace{\alpha_+ h_1(x_e, t - \frac{L_x - x}{\lambda_1(y)})}_{i} + \underbrace{\alpha_1 h_2(x_e, t - \frac{L_x - x}{\lambda_1(y)})}_{ii} + \underbrace{\alpha_2 h_1(x_e, t - \frac{L_x - x}{\lambda_2(y)})}_{iii} - \underbrace{\alpha_1 h_2(x_e, t - \frac{L_x - x}{\lambda_2(y)})}_{iv} \quad (12)$$

$$h_2(x, y, t) = \underbrace{\alpha_1 h_1(x_e, t - \frac{L_x - x}{\lambda_1(y)})}_{i} + \underbrace{\alpha_2 h_2(x_e, t - \frac{L_x - x}{\lambda_1(y)})}_{ii} - \underbrace{\alpha_1 h_1(x_e, t - \frac{L_x - x}{\lambda_2(y)})}_{iii} + \underbrace{\alpha_+ h_2(x_e, t - \frac{L_x - x}{\lambda_2(y)}),}_{iv} \quad (13)$$

where $\alpha_1 = \frac{1}{\sqrt{5}}$, $\alpha_2 = \frac{5-\sqrt{5}}{10}$, $\alpha_+ = \alpha_1 + \alpha_2$, x_e is the location of the eastern boundary, and L_x is the longitudinal extent of the domain. Any h_i terms evaluated at the eastern boundary no longer have latitudinal dependence because the assumed fast response sets the eastern boundary height regardless of y ; thus, $h_i(x, y, t)$ terms evaluated at the eastern boundary are written as $h_i(x_e, t)$.

The faster height adjustment in the top layer than the bottom layer is evident through examining the lag terms in Equations (12) and (13). We focus first on lag terms off the eastern boundary height in layer i which affect $h_j(x, y, t)$ for $i = j$. For these terms, there is a larger coefficient on the fast timescale in the top layer equation than the bottom layer equation (compare term i in Equation (12) to term ii in Equation (13)); there is a corresponding larger coefficient on the slow timescale in the bottom layer equation than the top layer equation (compare term iii in Equation (12) to term iv in Equation (13)). The remaining terms, which are lag terms off the eastern boundary in layer i which affect $h_j(x, y, t)$ for $i \neq j$, have the same coefficients ($\pm\alpha_1$) and do not account for a difference in adjustment.

The timescales λ_1 and λ_2 are determined by the long baroclinic Rossby wave speeds associated with the baroclinic modes in the 2.5-layer model (see Appendix C). Thus, the coefficient differences

noted above are equivalent to a larger projection of the faster mode onto the top layer than the bottom layer. This Rossby wave mechanism explains the faster propagation throughout the basin, visible in the upper ocean thickness adjustment, depending on the depth of the volume perturbation.

c. Time evolution of eastern boundary height

In Section 3b, we found an analytic solution for the propagation of information westward, which we are interpreting as governing interior upper ocean adjustment through lag equations off the eastern boundary height. Thus, we must also find the eastern boundary height timeseries, which we aim to relate to meridional fluxes in and out of the analytic domain. We will proceed with a general derivation without assuming equal thickness or reduced gravity between the two active layers, introducing $c_1(y) = \frac{\beta g'_1}{f^2}$ and $c_2(y) = \frac{\beta g'_2}{f^2}$.

We find the volume evolution at each latitude by zonally integrating Equation (7) from the eastern boundary (denoted x_e) to the edge of the western boundary current (denoted x_b), for each layer. We assume that the volume of the boundary region is small, i.e., that $\int_{x_w}^{x_e} h_i dx \approx \int_{x_b}^{x_e} h_i dx$, where x_w denotes the longitude of the western wall of the basin. Thus, the volume budget for each latitudinal band is:

$$\begin{aligned} \frac{\partial}{\partial t} \int_{x_w}^{x_e} h_1(x, y, t) dx &= H_1 c_2(y) [h_1(x_e, t) - h_1(x_b, y, t) + h_2(x_e, t) - h_2(x_b, y, t)] \\ &\quad + H_1 c_1(y) [h_1(x_e, t) - h_1(x_b, y, t)], \end{aligned} \quad (14)$$

$$\frac{\partial}{\partial t} \int_{x_w}^{x_e} h_2(x, y, t) dx = H_2 c_2(y) [h_1(x_e, t) - h_1(x_b, y, t) + h_2(x_e, t) - h_2(x_b, y, t)]. \quad (15)$$

As in Johnson and Marshall (2002), Equations (14) and (15) indicate that the layer thickness change at a given latitude depends on (zonal) volume fluxes. These fluxes propagate from the eastern boundary (terms of the form $H_i c_i h_i(x_e, t)$) and flow out of the interior of the basin at the western edge into the boundary current (terms of the form $-H_i c_i h_i(x_b, t)$).

We relate the volume evolution of each latitudinal band to meridional fluxes by zonally integrating the nonlinear continuity equations, using a no-normal flow condition at the walls, such that

$$\frac{\partial}{\partial t} \int_{x_w}^{x_e} h_i(x, y, t) dx = -\frac{\partial}{\partial y} T_i(y), \quad (16)$$

283 with $T_i(y) \equiv \int_{x_w}^{x_e} h_i v_i dx$ denoting the northward transport.

284 Thus, to find the full eastern boundary height, we can combine Equations (14), (15), and (16) and
 285 latitudinally integrate to write a volume budget for the analytic domain. This budget indicates that
 286 zonal fluxes (off the eastern boundary and eventually into the western boundary current) are equal
 287 to the difference in meridional fluxes at the southern and northern edges of the domain (denoted
 288 $T_{S,i}(t)$ and $T_{N,i}(t)$ respectively). The steps in this process are explicitly detailed in Appendix D2.
 289 Here, we show the final equations that can be solved for the eastern boundary heights in each layer
 290 as:

$$h_1(x_e, t) \int_0^{L_y} c_1(y) dy = \int_0^{L_y} c_1(y) h_1(x_b, y, t) dy + \frac{T_{S,1}(t)}{H_1} - \frac{T_{N,1}(t)}{H_1} - \frac{T_{S,2}(t)}{H_2} + \frac{T_{N,2}(t)}{H_2}, \quad (17)$$

$$\begin{aligned} h_2(x_e, t) \int_0^{L_y} c_2(y) dy &= -h_{1,e}(t) \int_0^{L_y} c_2(y) dy + \int_0^{L_y} c_2(y) (h_1(x_b, y, t) + h_2(x_b, y, t)) dy \\ &\quad + \frac{T_{S,2}}{H_2} - \frac{T_{N,2}}{H_2}. \end{aligned} \quad (18)$$

291 Equations (17) and (18) are solved iteratively together using that $h_i(x_b, y, t)$ is set by a time lag
 292 of $h_i(x_e, t)$ due to long baroclinic Rossby waves (see Equations (12) and (13)). In practice, we
 293 must avoid divergence of the integrals of $c_i(y)$ at the equator; here, we use that $H_i c_i(y) < 1$ (see
 294 Johnson and Marshall 2002). Taken together, Equations (17) and (18) can be fully solved given
 295 only northward fluxes at the north and south boundaries, which help set the eastern boundary
 296 heights; thus, these equations can be utilized to find the full adjustment of the interior h_i fields
 297 when combined with the theory in Section 3b. In the remainder of this subsection, we examine
 298 the meridional fluxes at the north and south boundaries (Section 3d) to complete the full analytical
 299 argument.

300 *d. Meridional fluxes at the edges of the domain*

301 The meridional transport at a given latitude, including the north or south boundaries, can be
 302 found by using $T_i(y) \equiv \int_{x_w}^{x_e} h_i v_i dx$ and assuming geostrophic balance. Thus, at a given latitude (y):

$$T_1(y, t) = \frac{g'_2 + g'_1}{2f} (h_1(x_e, t)^2 - h_1(x_w, y, t)^2) + \frac{g'_2}{f} \int_{x_w}^{x_e} \frac{dh_2}{dx} h_1 dx \quad (19)$$

$$T_2(y, t) = \frac{g'_2}{f} \int_{x_w}^{x_e} \frac{dh_1}{dx} h_2 dx + \frac{g'_2}{2f} (h_2(x_e, t)^2 - h_2(x_w, y, t)^2) \quad (20)$$

303 We simplify these expressions by noting that $\int_{x_w}^{x_e} \frac{dh_i}{dx} h_j dx \approx \int_{x_w}^{x_e} \frac{dh_i}{dx} h_i dx$ for $i \neq j$ as $h_i/h_j \approx 1$. For
 304 example, assessing this assumption numerically at the southern boundary, we find that the average
 305 deviation of h_i/h_j ($i \neq j$) from 1 is 0.005 and the largest deviation at any location and time across
 306 both top and bottom perturbation experiments is 0.030.

307
 308 Thus, we find the transport at both the northern and southern boundaries by using:

$$T_1(y, t) = \frac{g'_2 + g'_1}{2f} (h_1(x_e, t)^2 - h_1(x_w, y, t)^2) + \frac{g'_2}{2f} (h_2(x_e, t)^2 - h_2(x_w, y, t)^2) \quad (21)$$

$$T_2(y, t) = \frac{g'_2}{2f} (h_1(x_e, t)^2 - h_1(x_w, y, t)^2 + h_2(x_e, t)^2 - h_2(x_w, y, t)^2) \quad (22)$$

309 The value of the eastern boundary is used as found from Equations (17) and (18), while the
 310 western boundary thicknesses are diagnosed from the model. We note that this is similar to how
 311 the solution is closed in the 1.5-layer model in Johnson and Marshall (2002), where the western
 312 boundary thickness is prescribed at the southern edge of the domain and the outflow is prescribed
 313 at the northern edge. Here, we do not prescribe values so as to allow the dynamics to freely evolve.
 314 However, we utilize comparable information in the analytic theory, by diagnosing the time evolving
 315 western boundary layer thickness at both ends of the domain.

316 1) A POSSIBLE MECHANISM FOR THE FLUX DIFFERENCE AT THE SOUTHERN EDGE OF THE DOMAIN

317 Utilizing the western boundary layer thickness from the numerical model, as above, we can
 318 accurately represent the meridional transport at both the southern and northern boundaries using
 319 Equations (21) and (22). The regional upper ocean thickness is strongly dependent on these

320 meridional fluxes, especially at the southern boundary where the meltwater flows into the analytic
321 domain. In particular, there are larger northward fluxes at the southern boundary of the analytic
322 domain ($T_{S,i}(t)$) in a top-layer perturbation experiment compared to a bottom-layer perturbation
323 experiment.

324 We note that this difference in fluxes is also in agreement with the difference in long baroclinic
325 Rossby wave speeds that we found in Equations (12) and (13). The majority of the northward
326 transport out of the input region occurs in the western boundary current, which is generated by
327 the reflection of long Rossby waves as short Rossby waves which dissipate in the boundary region
328 (Pedlosky 1965). Thus, the western boundary current transport in each layer should be consistent
329 with the layer-wise differences in Rossby wave speeds derived in Section 3b. This reflection
330 mechanism is valid at all latitudes (e.g., see Marshall and Johnson 2013), although we draw
331 attention to it here at the southern boundary, to build intuition regarding the $T_{S,i}(t)$ terms.

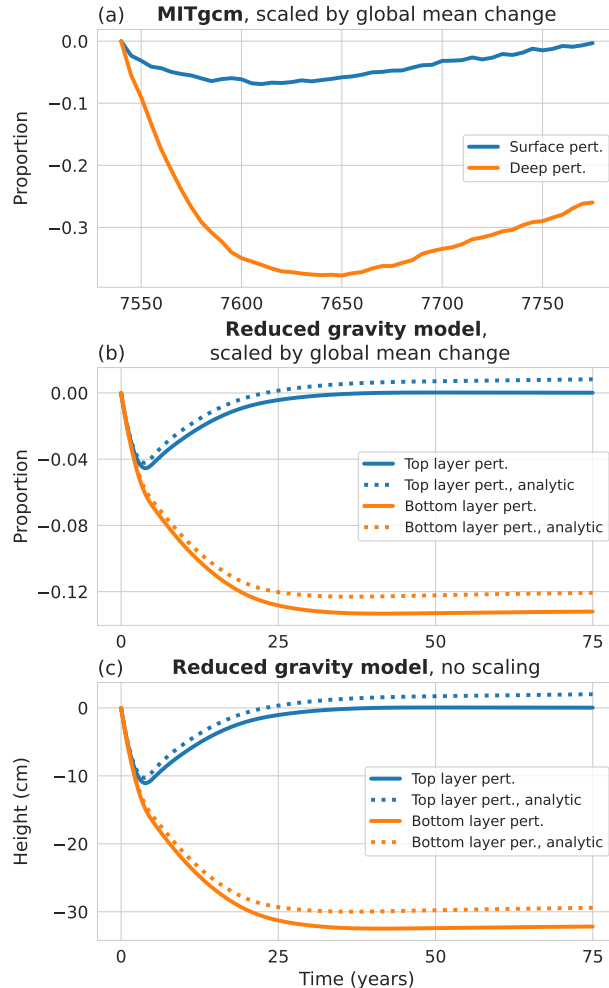
332 *e. Summary of theory for the dependence of adjustment on meltwater injection depth*

333 The theory derived throughout Section 3 suggests that variations in the regional adjustment of
334 volume anomalies in each density layer are due to layer-wise differences in long baroclinic Rossby
335 wave speeds. Initially, the eastern boundary adjusts due to transport north out of the volume input
336 region in a western boundary current which then travels to the eastern boundary as an equatorial
337 Kelvin wave. The magnitude of the volume transport in the western boundary current is inherently
338 linked to the Rossby wave propagation speed, leading to more transport into the analytic domain
339 in top-layer perturbation experiments. Then, the volume anomaly is propagated into the interior
340 through long baroclinic Rossby waves off the eastern boundary and this occurs more quickly in a
341 top-layer perturbation experiment.

351 The adjustment of the layer thicknesses in the interior of the basin through the Rossby wave
352 mechanism is visible in maps of the layer thicknesses in the analytic domain 75 years after the
353 volume input begins (Figures 4 and 5). The behavior of the numerical model is approximately
354 captured by the theory presented in Section 3, as can be seen by comparing the maps corresponding
355 to the analytic and numerical results. There is latitudinal dependence of the adjustment due to faster
356 long baroclinic Rossby wave speeds at lower latitudes (see the definitions of $\lambda_1(y)$ and $\lambda_2(y)$). The
357 larger h_1 thicknesses in the top-layer perturbation experiment (Figure 4) than h_2 in the bottom-layer

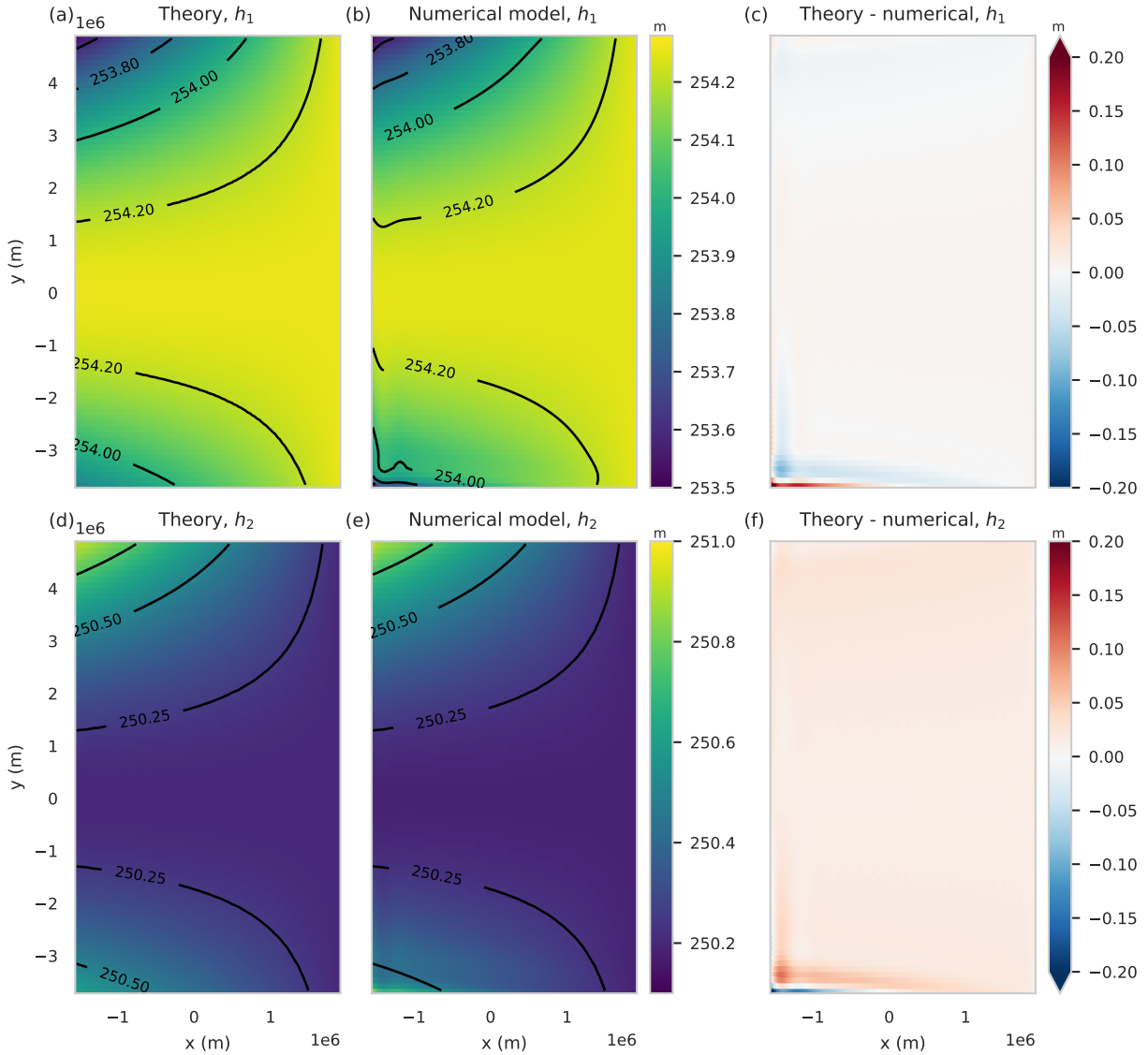
³⁵⁸ perturbation experiment (Figure 5) is consistent with the faster baroclinic Rossby waves in the top
³⁵⁹ layer than the bottom layer. This difference in the adjustment of each layer explains the difference
³⁶⁰ in the timeseries of the Northern Hemisphere upper ocean thickness anomaly originally shown in
³⁶¹ Figure 3b and c.

Change in Northern Hemisphere anomaly of upper ocean thickness



185 FIG. 3. Timeseries of Northern Hemisphere (NH) response to surface and deep meltwater perturbations. (a):
 186 upper ocean thickness in MITgcm run at 1° resolution in an idealized single basin domain, with surface or deep
 187 meltwater perturbations at the southern boundary (as in Eisenman et al. 2024). Here, upper ocean thickness is
 188 the amount of volume above a bounding isopycnal (as described in text). We plot the NH mean minus the global
 189 mean and scale it by the global mean change at year 110, which is approximately when the change in the system
 190 first equilibrates. The metric is smoothed with a 5-year moving average. (b): upper ocean thickness ($h_1 + h_2$) in
 191 the 2.5-layer reduced gravity model (Section 2a), including numerical (solid lines) and analytic solutions (dotted
 192 lines, see Section 3). We plot the NH mean minus the global mean and scale it by the global mean change at
 193 year 41, which is approximately when the change in the system first equilibrates. We focus on top or bottom
 194 layer perturbations, which is conceptually equivalent to surface or deep perturbations in MITgcm. (c): as panel
 195 (b), but without scaling by the global mean change; thus, this is simply the NH mean minus the global mean
 196 of $h_1 + h_2$. Note that the horizontal axis ranges are different between panel (a) and panels (b)/(c) due to faster
 197 response timescales in the simplified model. A comparable plot for panel (a) in the Southern Hemisphere would
 198 be equal and opposite; the same is true for panels (b)/(c), if one used the whole numerical domain for averaging.

Prediction throughout basin at 75 years with a top layer perturbation



342 **FIG. 4. Top** layer perturbation experiment comparisons of layer thicknesses (beginning from a resting ocean)
 343 between the analytical theory and 2.5-layer numerical model. Here, we utilize $g'_1 = g'_2 = g \frac{2}{1026}$ and $H_1 = H_2 =$
 344 250m. The region plotted is the analytic domain in Figure 2 (purple). Note that as shown on Figure 2, the
 345 analytic region crops out the western boundary current region to better see the adjustment of the interior of the
 346 basin. The left column, (a) and (d), shows the predicted layer thicknesses from analytic theory. The middle
 347 column, (b) and (e), shows the layer thicknesses from the numerical model. The right column, (c) and (f), shows
 348 the difference between the analytic prediction and the numerical model. The top row, (a), (b), and (c), shows
 349 quantities for the top layer height h_1 while the bottom row, (d), (e), and (f), shows the corresponding quantities
 350 for the bottom layer height h_2 .

Prediction throughout basin at 75 years with a bottom layer perturbation

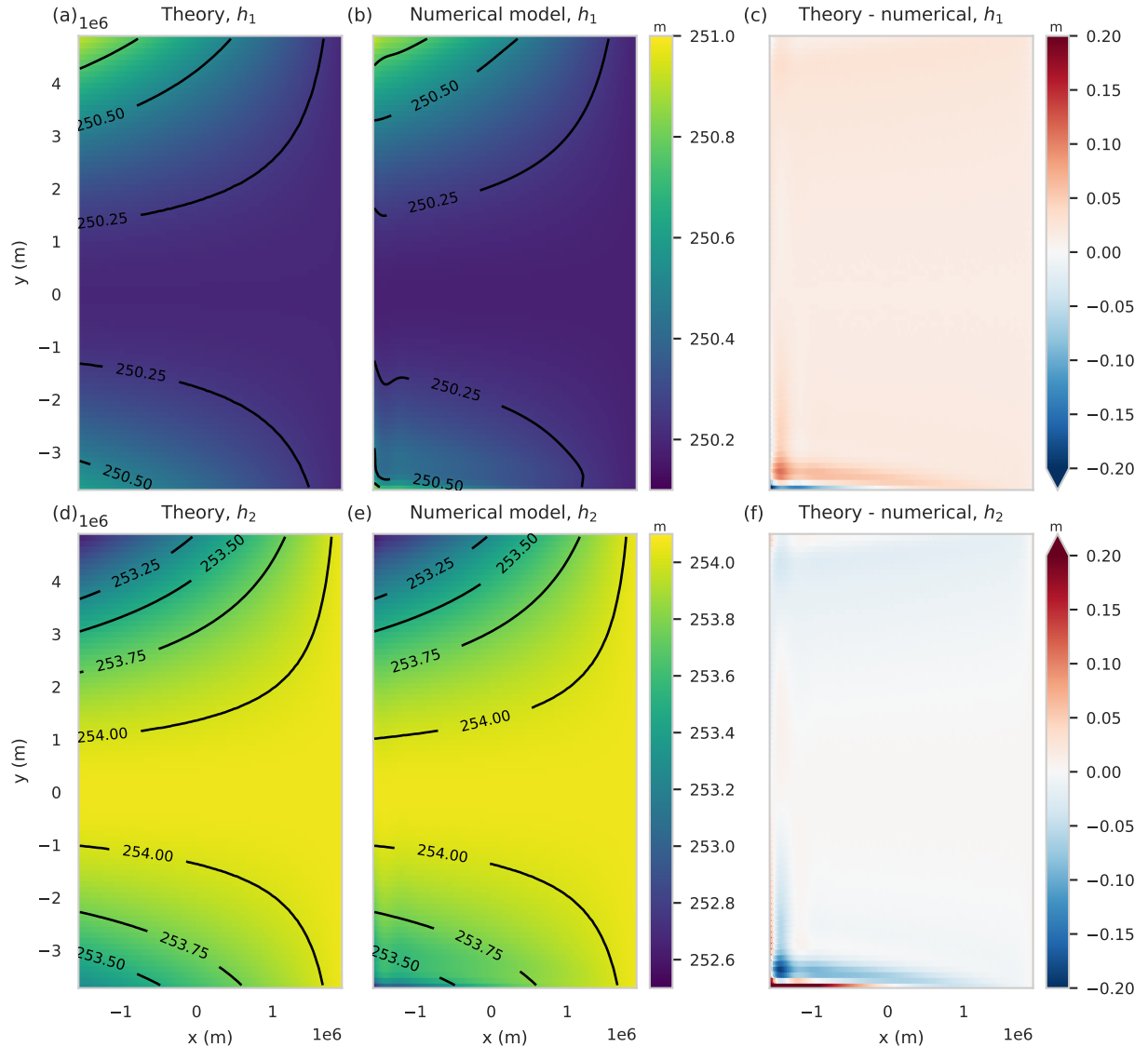


FIG. 5. As in Figure 4 but for a **bottom** layer perturbation experiment.

362 **4. Sensitivity to parameters and unresolved processes**

363 In this section, we explore the sensitivity of the results to (a) parameter choices such as layer
364 thicknesses and stratification and (b) an idealized representation of background transport induced
365 by wind. We comment on the extent to which the perturbed transport, for which we have developed
366 a theory, may help explain the upper ocean adjustment in more complex models.

367 *a. Layer thickness and stratification parameter choices*

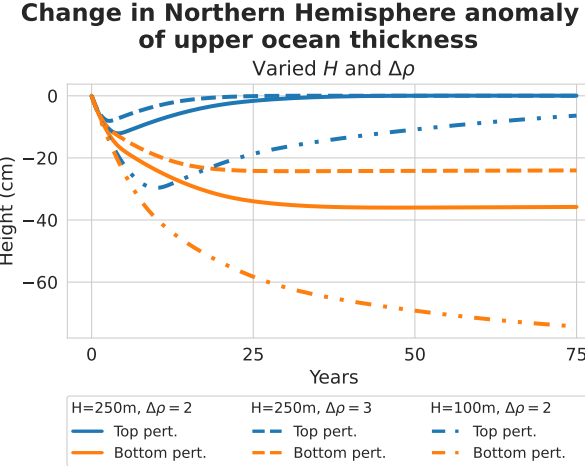
368 Faster adjustment of volume perturbations input into the top layer than the bottom layer holds
369 regardless of the choices of initial active layer thicknesses or stratification. However, different
370 quantitative responses in each layer can be achieved by changing these values, because the long
371 baroclinic Rossby wave speeds ($\lambda_1(y)$ and $\lambda_2(y)$) depend on H_1 , H_2 , g'_1 , and g'_2 .

372 1) CASE WHERE $H_1 = H_2$ AND $g'_1 = g'_2$

373 Here, we examine the case where the initial layer thicknesses of each active layer are the same
374 ($H \equiv H_1 = H_2$) and the density differences between each layer are the same such that $g' \equiv g'_1 = g'_2$.
375 The propagation of anomalies throughout the basin is faster for both layers with either larger layer
376 thicknesses H or density difference g' , as expected from $\lambda_1(y)$ and $\lambda_2(y)$, which governs the
377 evolution of the interior upper ocean volume (Equations (12) and (13)). As before, we evaluate
378 the difference in the adjustment timescales by examining the adjustment at the opposite end of
379 the basin from the meltwater input, indicated by the Northern Hemisphere upper ocean thickness
380 anomaly timeseries shown in the three set-ups in Figure 6. Compared to the parameter set-up of
381 $H = 250\text{m}$ and $g' = g \frac{2}{1026}$ (used in Figures 3b/c, 4, and 5), the adjustment of both layers is faster
382 for $H = 250\text{m}$ and $g' = g \frac{3}{1026}$ (dashed) and slower for $H = 100\text{m}$ and $g' = g \frac{2}{1026}$ (dash-dotted).

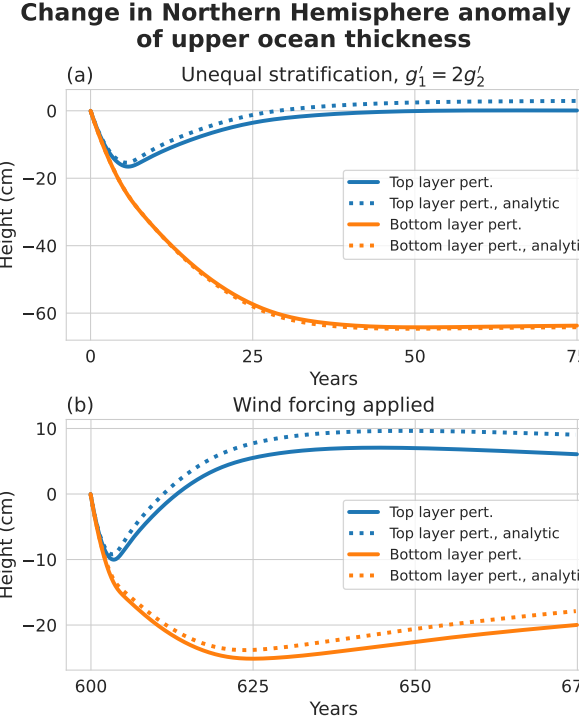
388 2) CASE WHERE $g'_1 \neq g'_2$

389 The stratification in the upper ocean is not generally uniform; thus, parameter choices in our
390 model closer to a realistic stratification would require $g'_1 > g'_2$. This choice leads to a larger
391 difference in the speed of adjustment between the two depths of perturbation, leading to a larger
392 difference in the Northern Hemisphere upper ocean thickness anomaly than for equal reduced
393 gravities (Figure 7a). This can be understood using Equations (D6) and (D7), where we derive



383 FIG. 6. Numerical 2.5-layer model Northern Hemisphere upper ocean thickness anomaly for simulations with
 384 an ocean initially at rest and $H \equiv H_1 = H_2$ and $g' \equiv g \frac{\Delta\rho}{\rho_0} \equiv g'_1 = g'_2$, with a range of H and g' choices (see legend).
 385 The solid lines shown here are equivalent to the standard parameter set-up explored in this paper (i.e., that used
 386 in Figure 3b/c). It holds that the adjustment in each layer is slower due to either smaller H or smaller g' . A
 387 comparable plot for the Southern Hemisphere would be equal and opposite.

394 analogues to Equations (12) and (13) without assuming $g'_1 = g'_2$ and $H_1 = H_2$. Here, we see that
 395 with $g'_1 > g'_2$, there are larger coefficients on the fast timescale and smaller coefficients on the slow
 396 timescale in the top layer. This is reversed in the lower layer, such that larger coefficients are on
 397 the slow timescale. We note that the timescales themselves also change such that the difference in
 398 $\lambda_1(y)$ and $\lambda_2(y)$ is also larger when $g'_1 > g'_2$ than when $g'_1 = g'_2$. Thus, the quantitative difference in
 399 adjustment timescales, indicated by the Northern Hemisphere upper ocean thickness anomaly, is
 400 dependent on parameter choices, which can be understood by the corresponding faster adjustment
 401 in the top layer due to baroclinic Rossby wave propagation (see the analytic solution in Figure 7a).



402 FIG. 7. 2.5-layer model Northern Hemisphere upper ocean thickness anomaly, including numerical and
 403 analytical results, for (a) simulations with an ocean initially at rest and $H_1 = H_2 = 250\text{m}$ and $g'_1 = 2g'_2$ and (b)
 404 simulations with wind applied and $H_1 = H_2 = 250\text{m}$ and $g'_1 = g'_2$. In panel (b), the results are plotted for 75 years
 405 of volume input following 600 years of spin-up with wind applied.

406 *b. The effect of wind*

407 The 2.5-layer model, run from a resting state as we've examined thus far, is an idealized represen-
 408 tation of processes which propagate the volume anomaly due to perturbed transport induced by the
 409 meltwater itself. However, in a more realistic model set-up, we expect the background transport,
 410 absent here, will also advect the new meltwater anomaly. For example, we may expect that the
 411 Ekman transport driven by wind forcing may advect the anomaly more strongly in the top active
 412 layer than the bottom active layer. Here, we use a set-up (see Figure 2a) which approximately
 413 mirrors the set-up in MITgcm, where the wind was imposed in a circumpolar current region with a
 414 re-entrant channel, and examine the effect of background transport induced by wind in the 2.5-layer
 415 model. We note that while the wind forcing in this idealized model is not realistic, especially given
 416 that the meltwater input is further north than in the MITgcm model due to the sponge layers, it is

417 sufficient to demonstrate the potential impact of a background transport on the meltwater anomaly.
418 In these runs, we use the same layer thicknesses and reduced gravities as for the results presented
419 in Figure 3b/c. First, we spin-up the ocean for 600 years with an imposed wind forcing, but without
420 a meltwater anomaly. We then create two experiments starting from the end of the control, where
421 meltwater is introduced into either the top or bottom active layer.

422 Figure 7b shows the Northern Hemisphere upper ocean thickness anomaly in the experiments
423 with wind imposed; here, we have plotted the difference from the end of the spin up run with
424 just wind applied. We find stronger anomalies in both experiments in the Northern Hemisphere
425 compared to the experiments where meltwater is input into a resting ocean due to the additional
426 Ekman transport propagating the anomaly. During the initial adjustment (the first ~ 25 years), the
427 difference between the Northern Hemisphere upper ocean thickness anomaly in each experiment
428 (top- or bottom-layer perturbation) is also slightly larger; this is because the wind more strongly
429 affects transport in the top active layer. This difference reverses after equilibration of the initial
430 response because there is more volume near where the wind is imposed in a bottom-layer experiment
431 due to the initially slower response.

432 In Figure 7b, we also show the analytic solution, which largely captures the numerical results.
433 Importantly, this analytic solution is possible because the wind is applied south of the analytic
434 domain. Thus, the impact on the analytic domain is only through the $T_{s,1}$ and $T_{s,2}$ terms. If the
435 wind were applied in the interior, the analytic solution would need to be modified to account for
436 Ekman transport, as was done in a 1.5-layer model in Zhai et al. (2014). However, a modification of
437 the analytic solution in the 2.5 layer case would not straightforwardly follow the treatment in Zhai
438 et al. (2014), as the wind would induce a mean flow in both layers, which results in a Doppler shift
439 of the Rossby wave speeds associated with a given mode dependent on the mean flow associated
440 with both layers (e.g., Liu 1999).

441 We conclude that the adjustment of the volume anomalies throughout the basin will be affected by
442 a background circulation. For example, the effect of wind may account for an additional difference
443 between the dynamic adjustment of volume anomalies in the top layer compared to the bottom
444 layer of the 2.5-layer reduced gravity model during the initial adjustment of the volume anomalies.

445 **5. Conclusion**

446 Antarctica has been losing mass during recent decades (e.g., Otosaka et al. 2023), with additional
447 mass loss projected regardless of emissions scenario over the coming century (e.g., Lowry et al.
448 2021). Sea level rise from ice sheet mass loss will not be globally uniform, in part due to ocean
449 dynamic processes (e.g., Stammer 2008; Lorbacher et al. 2012; Kopp et al. 2010; Schmidt et al.
450 2023). Thus, reliable modelling of the ocean's response to meltwater is crucial for predicting
451 the temporal evolution of regional sea level changes. Current projections of sea level rise due to
452 meltwater from ice sheets are typically performed with hosing experiments, where meltwater is
453 input at the surface in an atmosphere-ocean model with a prescribed horizontal distribution and
454 temporal modulation. However, observational evidence suggests that Antarctic meltwater comes
455 primarily from basal melt of ice shelves, and it turbulently mixes as it exits the ice shelf cavity
456 and enters the water column considerably below the surface (Kim et al. 2016; Garabato et al.
457 2017). Thus, there are important unanswered questions about the sensitivity of regional sea level
458 projections and their evolution in time to the vertical distribution of meltwater input.

459 In preliminary work, we have demonstrated in an idealized single basin model set-up with
460 MITgcm that the dynamic sea level depends on the depth of meltwater input (Eisenman et al.
461 2024). In particular, there is more dynamic sea level rise at opposite end of the basin (i.e., in
462 the Northern Hemisphere) and less near the input location (i.e., in the Southern Hemisphere) in
463 response to an idealized Southern Ocean volume input at the surface than at depth. In the present
464 study, we first demonstrated that this result stems from the upper ocean thickness adjustment,
465 which has faster adjustment of the Northern Hemisphere (relative to the global mean) in a surface
466 perturbation experiment than a deep perturbation experiment. Thus, we focused on a 2.5-layer
467 model and presented an associated theory that captures the key dynamics of adjustment in order to
468 interpret the MITgcm results. We have focused on the response of the upper ocean volume transport
469 and how these dynamic processes vary with depth. We have found that the upper ocean volume
470 adjusts faster throughout the basin (indicated by the Northern Hemisphere mean) in response
471 to a top-layer perturbation compared to a bottom-layer perturbation. This is due to the vertical
472 dependence of baroclinic Rossby waves, which determine the response of the signal propagation
473 around the basin on multidecadal (and longer) timescales.

474 For the theory developed in this paper, we rely on dynamic ocean mechanisms presented in
475 previous studies using reduced gravity models to investigate the response to changes in forcing
476 such as: changes in wind (e.g., Cessi and Otheguy 2003; Zhai et al. 2014), changes in deep
477 water formation (e.g., Kawase 1987; Huang et al. 2000; Johnson and Marshall 2002, 2004; Cessi
478 et al. 2004; Zhai et al. 2011; Nieves and Spall 2018; Sun et al. 2020), and heat sources in the
479 North Atlantic and Southern Ocean (e.g., Hsieh and Bryan 1996). In particular, we assume that
480 there is a fast response from both the western boundary current and Kelvin waves, followed by a
481 slow response governed by Rossby waves emanating off the eastern boundary. This mechanism
482 has also been noted in the response of more complex ocean GCMs to changes in deep water
483 formation (e.g., Goodman 2001; Cessi et al. 2004) or meltwater forcing (Stammer 2008). The key
484 difference between the theory in this paper and previously presented theories for other phenomena
485 that also relied on reduced gravity models is that we investigate the vertical dependence of a volume
486 perturbation by utilizing a second active layer in the model.

487 While the adjustment mechanism that we identify involving the vertical dependence of baroclinic
488 Rossby waves is expected to play a key role in explaining the baroclinic adjustment of more complex
489 models (e.g., Eisenman et al. 2024), other processes not captured in our idealized theory may also
490 affect the results. In particular, the background circulation, which is driven by wind and buoyancy
491 forcing, will influence the propagation of the volume input. We examined a simplified version
492 of the effect of wind forcing on our result and found that it induces: (1) larger (more positive)
493 volume anomalies at the opposite end of the basin from volume input (Northern Hemisphere) on
494 multidecadal timescales regardless of the depth of perturbation; and (2) a larger difference of the
495 Northern Hemisphere upper ocean thickness anomaly between the surface and deep perturbations
496 during the initial adjustment period. A more realistic inclusion of wind forcing, as well as the
497 inclusion of other processes that are not accounted for here, such as an upper cell meridional
498 overturning circulation, is expected to also influence the response throughout the basin to surface
499 versus deep perturbations on multidecadal timescales. In addition to the background transport in
500 the upper ocean, recent work has demonstrated an expected slowdown of the abyssal overturning
501 due to the shutdown of Antarctic deep water formation driven by ice sheet meltwater (e.g., Lago
502 and England 2019; Li et al. 2023a). As shown explicitly in Lago and England (2019), the change
503 in the abyssal circulation will have an impact on the sea surface height field, largely from the steric

504 signal. In this work, we have assumed the abyss to be motionless and focused only on upper ocean
505 dynamics. Thus, we do not account for this effect or the possible influence of changes in the abyssal
506 cell depending on the depth of meltwater input (visible in Figure S7 of Eisenman et al. 2024). In
507 addition to omitting background transport in both the upper and abyssal ocean, the idealized model
508 presented here may differ from more complex models and real world ocean adjustment because the
509 2.5-layer model: (1) has different and more simplified stratification than is realistic; (2) is solved on
510 a Cartesian grid rather than in latitude-longitude space; and (3) only properly captures the expected
511 impact of upper ocean dynamic processes, and not the contribution of the abyss (see Appendix B2).
512 However, the theory presented here provides a mechanistic understanding of physical processes
513 which may contribute to the dependence of the time-evolving sea level pattern on meltwater input
514 depth. This dependence may lead to errors in sea level projections that adopt the current standard
515 approach for prescribing meltwater fluxes.

516 *Acknowledgments.* This work was supported by NSF OCE grants 2048576 and 2048590. We
517 thank Pavel Perezhogin for helpful discussions on the numerics, as well as David Marshall and an
518 anonymous reviewer for their feedback which helped improve the manuscript. This work was also
519 supported by the New York University IT High Performance Computing resources, services, and
520 staff expertise.

521 *Data availability statement.* The code utilized to make all figures in this paper is publicly available
522 at https://github.com/aurora-bf/2.5_layer_model. By the time of publication, the code
523 will be associated with a DOI by uploading it to Zenodo. The underlying numerical 2.5-layer model
524 is a significantly modified version of an existing single layer shallow water code (Penn and Vallis
525 2018); some of the modifications include changing the equations solved and adding a different
526 time-stepping method.

527 APPENDIX

528 APPENDIX A

529 Numerical details for the 2.5-layer model

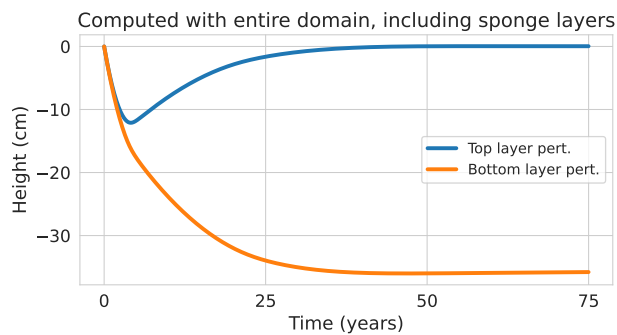
530 Numerically, Equations (1) and (2) are solved with finite differences in space on an Arakawa-C
531 grid such that the h_i quantities are located at the center of the cell, the v_i quantities are located at the
532 north and south edges, and the u_i quantities are located at the east and west edges. The equations
533 are integrated in time using the 4th order Runge-Kutta method with a timestep of 250 seconds. The
534 domain is rectangular with size 3.796×10^6 meters in the zonal direction and 1.379×10^7 meters
535 in the meridional direction (see exact dimensions with more significant digits in associated code).
536 We utilize 128 and 129 grid points in the zonal and meridional directions respectively. The domain
537 size was chosen such that the total area is the same as in MITgcm, so that a 0.1 Sv perturbation
538 causes the same global mean volume increase in each model.

539 We use no-slip and no-normal flow boundary conditions at the edges of the domain to represent
540 solid boundaries. The no-slip condition is implemented using a ghost cell approach (following, e.g.,
541 Adcroft and Marshall 1998). We include sponge layers, implemented as a linear drag (Rayleigh
542 friction), at the north and south ends of the domain to damp out gravity waves. Each sponge layer

543 is effective over 18 grid points, with a strength profile that decays exponentially away from the
 544 boundary using a decay scale of 5 grid points and a maximum friction coefficient of $r = 10^{-4}\text{s}^{-1}$.
 545 In simulations where wind is imposed, a re-entrant channel region is utilized to maintain the flow
 546 (see Figure 2b); in the channel region, periodic boundary conditions are used rather than no-slip
 547 and no-normal flow conditions.

552 In the main text, the timeseries in the Northern Hemisphere is calculated using the analytic
 553 domain indicated in Figure 2b. Here, in Figure A1, we show a comparable plot to Figure 3c,
 554 but over the whole numerical domain; we find that this change only makes a small quantitative
 difference.

Change in Northern Hemisphere anomaly of upper ocean thickness



548 FIG. A1. Numerical 2.5-layer model Northern Hemisphere upper ocean thickness anomaly for simulations
 549 with an ocean initially at rest and $H_1 = H_2 = 250\text{m}$ and $g'_1 = g'_2$. This plot is comparable to the numerical result
 550 plotted in Figure 3c, except the whole numerical domain is used when taking the Northern Hemisphere mean. A
 551 comparable plot for the Southern Hemisphere would be equal and opposite.
 555

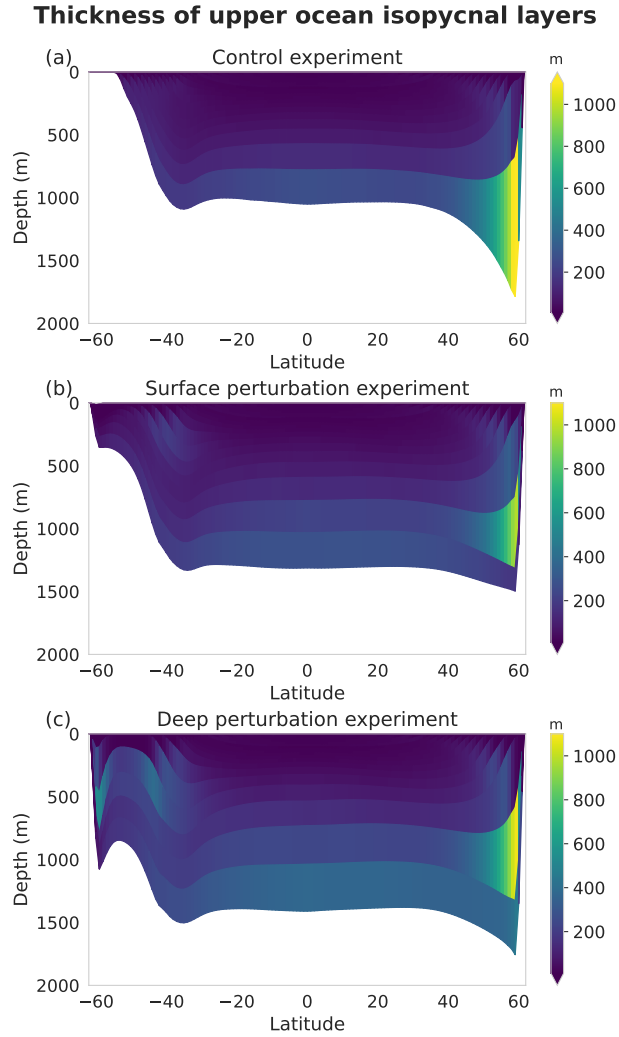
APPENDIX B

Depths of isopycnals in each model

B1. Upper ocean thickness in MITgcm

559 In Figure B1, we show the zonally averaged depth of the isopycnal chosen to define the upper
 560 ocean. Thus, the deepest depth plotted in this figure is equivalent to the upper ocean thickness used

561 throughout the paper. It is visible that the isopycnal chosen to define the upper ocean correlates to
 562 around 1000m in the midlatitudes in the control simulation (panel a).



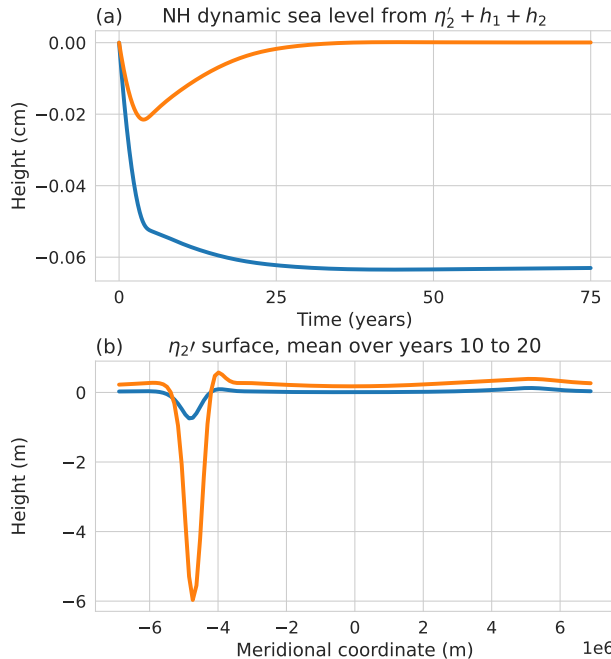
563 FIG. B1. The thickness of isopycnal layers over the last 50 years of simulation. The layers are plotted in
 564 z -space, by projecting the location of the isopycnal back to the appropriate depth using the cumulative sum of
 565 the thickness of isopycnal layers above. Here, we plot only the isopycnal layers defined to make up the upper
 566 ocean throughout the paper. Thus, the deepest depth of the plotted isopycnals is equivalent to the thickness of the
 567 upper ocean (Equation (4)). (a): control experiment, (b): surface perturbation experiment, (c): deep perturbation
 568 experiment.

569 **B2. 2.5-layer model sea level**

570 The sea level in the 2.5-layer model can be found by solving for the height of the isopycnal
 571 separating the active fluid from the abyssal layer (denoted η_2) and then taking the sea level ζ as $\zeta =$
 572 $\eta_2 + h_2 + h_1$. Using that there is no pressure gradient in the abyss, we find that $\eta_2 = \frac{-\rho_1 h_1 - \rho_2 h_2}{\rho_3} + C(t)$,
 573 where $C(t)$ is chosen such that the global mean η_2 relative to the bottom of the stacked fluid is
 574 constant in time. We write η_2 as $\eta_2 = <\eta_2> + \eta'_2$ where $<\eta_2>$ is prescribed as the global mean
 575 height of the abyss (unchanged in time) and η'_2 is deviations from this:

$$\eta'_2 = \frac{-\rho_1 h_1 - \rho_2 h_2}{\rho_3} - \frac{\overline{-\rho_1 h_1 - \rho_2 h_2}}{\rho_3}. \quad (\text{B1})$$

Isopycnal surfaces between experiments



576 FIG. B2. Isopycnal surfaces in simulations with an ocean initially at rest and $H_1 = H_2 = 250$ m and $g'_1 = g'_2$.
 577 (a): model sea level over time, calculated as $\eta'_2 + h_1 + h_2$. This plot is comparable to the numerical result plotted
 578 in Figure 3c, except the model sea level is plotted rather than the sum of the active layer thicknesses. (b): the
 579 time-mean depth of η'_2 from years 10 to 20 plotted against latitude. Thus, this plot can be used to understand the
 580 difference in the model free surface compared to the upper ocean thickness focused on in the main text.

581 We solve for the dynamic sea level using η'_2 and the h_1 and h_2 quantities (Figure B2a). This
582 dynamic sea level is equivalent to the steric sea level.

583 In this paper, we found that the upper ocean transport results in faster propagation of the volume
584 anomalies to the opposite end of the basin (Northern Hemisphere) when inputting volume in the
585 top active layer, but the model sea level shows larger Northern Hemisphere sea level when inputting
586 volume into the bottom active layer. This is because the abyss is motionless and the η_2 isopycnal
587 responds to the weight of the fluid above it. In a bottom-layer perturbation experiment, due to slower
588 propagation of the volume anomalies, more fluid stays in the input region, depressing η'_2 more in
589 this location than in a top-layer perturbation experiment. This results in the isopycnal elsewhere
590 becoming more positive due to the requirement of a global mean of 0 (see Figure B2b). Thus,
591 this regional η'_2 structure is due to the slower upper ocean transport in a bottom-layer perturbation
592 experiment than a top-layer perturbation experiment. The sum of the regional height of η'_2 versus
593 the regional height of $h_1 + h_2$ nearly cancel out as evidenced by the very small values in Figure
594 B2a, but the response of η'_2 is slightly more dominant. However, in a more realistic model, the
595 abyss may have its own dynamics, and the spatial structure of the η_2 isopycnal would be set by
596 additional processes, unaccounted for in the 2.5-layer model, including mixing and both the upper
597 and abyssal ocean background state and transport.

598 Despite the small sea level signal in the 2.5-layer model that does not match the MITgcm sea
599 level, the upper ocean transport investigated in this model is relevant to the MITgcm sea level result
600 because the mechanism of differing speeds of baroclinic Rossby waves with depth is expected to
601 hold and contribute to sea level adjustment. In particular, we demonstrated that the upper ocean
602 thickness adjustment drives the faster adjustment of regional sea level with surface meltwater input
603 (compared to deep meltwater input) in MITgcm.

604

APPENDIX C

605 Rossby wave speeds associated with baroclinic modes

606 The 2.5-layer model has two baroclinic modes (e.g., Vandermeirsch et al. 2003). The potential
607 vorticity in each layer can be modified from the classic 2-layer equations to add the half-layer

608 dynamics. They are as follows:

$$q_1 = f_0 + \beta y + \nabla^2 \psi_1 + F_1(\psi_2 - \psi_1) \quad (\text{C1})$$

$$q_2 = f_0 + \beta y + \nabla^2 \psi_2 + F_2(\psi_1 - \psi_2) - F_3 \psi_2 \quad (\text{C2})$$

609 where $F_1 = \frac{f^2}{g'_1 H_1}$, $F_2 = \frac{f^2}{g'_2 H_2}$, and $F_3 = \frac{f^2}{g'_2 H_2}$. Here, we demonstrate the case of equal reduced
610 gravities and mean layer thicknesses, i.e., $F_1 = F_2 = F_3$, which we denote as F .

611 We make the planar wave assumption ($\psi_i = \tilde{\psi}_i e^{i(kx+ly-\omega t)}$) and set-up the time evolution partial
612 differential equations for q_i :

$$\omega((k^2 + l^2) - F(\tilde{\psi}_2 - \tilde{\psi}_1)) + k\beta\tilde{\psi}_1 = 0 \quad (\text{C3})$$

$$\omega((k^2 + l^2) - F(\tilde{\psi}_1 - \tilde{\psi}_2) + F\tilde{\psi}_2) + k\beta\tilde{\psi}_2 = 0 \quad (\text{C4})$$

613 We solve an eigenvalue problem based on Equations (C3) and (C4) for Γ such that $\omega((k^2 + l^2) +$
614 $\Gamma)\tilde{\psi} + \beta k\tilde{\psi} = 0$ where $\tilde{\psi} = [\tilde{\psi}_1, \tilde{\psi}_2]$. Here, Γ is κ_D^2 , the inverse of the deformation radius, and
615 $\omega = -\frac{\beta k}{(k^2 + l^2) + \Gamma}$.

616 We find that $\kappa_D^2 = \frac{1}{L_D^2} = \frac{3 \pm \sqrt{5}}{2} F$. We choose the baroclinic modes such that $L_{D,1} > L_{D,2}$ which
617 means $\kappa_{D,1}^2 = \frac{f^2}{g'H} \frac{3-\sqrt{5}}{2}$ and $\kappa_{D,2}^2 = \frac{f^2}{g'H} \frac{3+\sqrt{5}}{2}$.

618 Thus, using that the long Rossby wave group velocity in the x direction is $c_g^x = \frac{\beta}{\kappa_D^2}$, we find:

$$\begin{aligned} c_{g,1}^x &= \frac{\beta g' H}{f^2} \frac{2}{3 - \sqrt{5}} \\ &= \frac{\beta g' H}{f^2} \frac{3 + \sqrt{5}}{2} \end{aligned} \quad (\text{C5})$$

$$\begin{aligned} c_{g,2}^x &= \frac{\beta g' H}{f^2} \frac{2}{3 + \sqrt{5}} \\ &= \frac{\beta g' H}{f^2} \frac{3 - \sqrt{5}}{2} \end{aligned} \quad (\text{C6})$$

619 These long Rossby wave speeds are $\lambda_1(y)$ and $\lambda_2(y)$ presented in Section 3b.

620

APPENDIX D

621

More details on and extension to the theory

622 **D1. Theory where the heights and reduced gravities are not equal between layers**

623 In Section 3b, we derived an analytic equation that governs transport off the eastern boundary. We
 624 assumed that $g'_1 = g'_2$ and $H_1 = H_2$ to simplify interpretation in text. Here, we show an equivalent
 625 derivation without this assumption.

626 The system can be written as in Equation 8, but with

$$\mathbf{A} = \begin{bmatrix} H_1(c_1(y) + c_2(y)) & H_1c_2(y) \\ H_2c_2(y) & H_2c_2(y) \end{bmatrix} \quad (\text{D1})$$

627 where $c_i(y) = \frac{\beta g'_i}{f^2}$. Dropping y dependences of c_i in the notation, the eigenvalues of the matrix are:

$$\lambda_1(y) = \frac{H_2c_2 + H_1(c_1 + c_2)}{2} + \frac{B}{2} \quad (\text{D2})$$

$$\lambda_2(y) = \frac{H_2c_2 + H_1(c_1 + c_2)}{2} - \frac{B}{2} \quad (\text{D3})$$

628 where $B = \sqrt{(-H_2c_2 - H_1(c_1 + c_2))^2 - 4H_1H_2c_1c_2}$. We diagonalize with $\Lambda = \mathbf{P}\mathbf{A}\mathbf{P}^{-1}$ and

$$\mathbf{P} = \frac{H_2c_2}{B} \begin{bmatrix} 1 & \frac{1}{2} - \frac{H_1(c_1+c_2)}{2H_2c_2} + \frac{B}{2H_2c_2} \\ -1 & -\frac{1}{2} + \frac{H_1(c_1+c_2)}{2H_2c_2} + \frac{B}{2H_2c_2} \end{bmatrix} \quad (\text{D4})$$

$$= \frac{H_2c_2}{B} \begin{bmatrix} 1 & F \\ -1 & G \end{bmatrix} \quad (\text{D5})$$

629 with $F = \frac{1}{2} - \frac{H_1(c_1+c_2)}{2H_2c_2} + \frac{B}{2H_2c_2}$ and $G = -\frac{1}{2} + \frac{H_1(c_1+c_2)}{2H_2c_2} + \frac{B}{2H_2c_2}$. Using the same process as in Section
 630 3b , we find

$$h_1(x, y, t) = \frac{GH_2c_2}{B} h_1(x_e, t - \frac{L_x-x}{\lambda_1(y)}) + \frac{FGH_2c_2}{B} h_2(x_e, t - \frac{L_x-x}{\lambda_1(y)}) \\ + \frac{FH_2c_2}{B} h_1(x_e, t - \frac{L_x-x}{\lambda_2(y)}) - \frac{FGH_2c_2}{B} h_2(x_e, t - \frac{L_x-x}{\lambda_2(y)}) \quad (\text{D6})$$

$$h_2(x, y, t) = \frac{H_2c_2}{B} h_1(x_e, t - \frac{L_x-x}{\lambda_1(y)}) + \frac{FH_2c_2}{B} h_2(x_e, t - \frac{L_x-x}{\lambda_1(y)}) \\ - \frac{H_2c_2}{B} h_1(x_e, t - \frac{L_x-x}{\lambda_2(y)}) + \frac{GH_2c_2}{B} h_2(x_e, t - \frac{L_x-x}{\lambda_2(y)}). \quad (\text{D7})$$

631 This equation is applied and tested in Section 4a.2.

632 **D2. Additional details to find the eastern boundary heights**

633 In Section 3c, we derive how to find the eastern boundary height in terms of meridional fluxes at
634 the north and south ends of the domain. Here, we explicitly write out the steps between Equation
635 (16) and Equations (17) and (18).

636 We substitute Equation (16) into Equations (14) and (15):

$$-\frac{\partial}{\partial y} T_1(y, t) = H_1 c_2(y) [h_1(x_e, t) - h_1(x_b, y, t) + h_2(x_e, t) - h_2(x_b, y, t)] \\ + H_1 c_1(y) [h_1(x_e, t) - h_1(x_b, y, t)], \quad (\text{D8})$$

$$-\frac{\partial}{\partial y} T_2(y, t) = H_2 c_2(y) [h_1(x_e, t) - h_1(x_b, y, t) + h_2(x_e, t) - h_2(x_b, y, t)], \quad (\text{D9})$$

637 to write a volume budget relating the meridional and zonal volume fluxes at each latitude. We
638 write a volume budget for the whole analytic domain by latitudinally integrating Equations (D8)
639 and (D9):

$$h_1(x_e, t) \int_0^{L_y} (c_1(y) + c_2(y)) dy + h_2(x_e, t) \int_0^{L_y} c_2(y) dy = \\ \int_0^{L_y} (c_1(y) + c_2(y)) h_1(x_b, y, t) dy + \int_0^{L_y} c_2(y) h_2(x_b, y, t) dy + \frac{T_{S,1}(t)}{H_1} - \frac{T_{N,1(t)}}{H_1}, \quad (\text{D10})$$

$$h_1(x_e, t) \int_0^{L_y} c_2(y) dy + h_2(x_e, t) \int_0^{L_y} c_2(y) dy = \\ \int_0^{L_y} c_2(y) h_1(x_b, y, t) dy + \int_0^{L_y} c_2(y) h_2(x_b, y, t) dy + \frac{T_{S,2}(t)}{H_2} - \frac{T_{N,2(t)}}{H_2}, \quad (\text{D11})$$

640 using $T_{S,i}(t)$ and $T_{N,i}(t)$ as defined in text. The equations that we solve iteratively for the eastern
641 boundary heights (Equation (17) and (18)) are rearrangements of the set of Equations (D10) and
642 (D11).

643 **References**

644 Adcroft, A., and D. Marshall, 1998: How slippery are piecewise-constant coastlines in numerical
645 ocean models? *Tellus A: Dynamic Meteorology and Oceanography*, **50** (1), 95–108,
646 <https://doi.org/10.3402/TELLUSA.V50I1.14514>.

- 647 Adusumilli, S., H. A. Fricker, B. Medley, L. Padman, and M. R. Siegfried, 2020: Interan-
648 nual variations in meltwater input to the Southern Ocean from Antarctic ice shelves. *Nature*
649 *Geoscience 2020 13:9*, **13 (9)**, 616–620, <https://doi.org/10.1038/s41561-020-0616-z>, URL
650 <https://www.nature.com/articles/s41561-020-0616-z>.
- 651 Bronselaer, B., M. Winton, S. M. Griffies, W. J. Hurlin, K. B. Rodgers, O. V. Sergienko, R. J.
652 Stouffer, and J. L. Russell, 2018: Change in future climate due to Antarctic meltwater. *Nature*,
653 **564**, 53–58, <https://doi.org/10.1038/s41586-018-0712-z>.
- 654 Cane, M. A., and S. E. Zebiak, 1985: A Theory for El Niño and the Southern Oscillation. *Science*,
655 **228 (4703)**, 1085–1087, <https://doi.org/10.1126/SCIENCE.228.4703.1085>.
- 656 Cessi, P., K. Bryan, and R. Zhang, 2004: Global seiching of thermocline waters between the Atlantic
657 and the Indian-Pacific Ocean Basins. *Geophysical Research Letters*, **31 (4)**, <https://doi.org/10.1029/2003GL019091>.
- 658 Cessi, P., and P. Otheguy, 2003: Oceanic Teleconnections: Remote Response to Decadal Wind
659 Forcing. *Journal of Physical Oceanography*, **33 (8)**, 1604–1617, <https://doi.org/10.1175/2400.1>.
- 660 Chang, P., Y. Fang, R. Saravanan, L. Ji, and H. Seidel, 2006: The cause of the fragile relationship
661 between the Pacific El Niño and the Atlantic Niño. *Nature*, **443**, 324–328, <https://doi.org/10.1038/nature05053>.
- 662 Depoorter, M. A., J. L. Bamber, J. A. Griggs, J. T. M. Lenaerts, S. R. M. Ligtenberg, M. R. Van
663 Den Broeke, and G. Moholdt, 2013: Calving fluxes and basal melt rates of Antarctic ice shelves.
Nature, **502**, 89–92, <https://doi.org/10.1038/nature12567>.
- 664 Eisenman, I., A. Basinski-Ferris, E. Beer, and L. Zanna, 2024: The Sensitivity of the Spatial
665 Pattern of Sea Level Changes to the Depth of Antarctic Meltwater Fluxes. *Geophysical Research*
666 *Letters*, **51 (19)**, <https://doi.org/10.1029/2024GL110633>.
- 667 Eyring, V., S. Bony, G. A. Meehl, C. A. Senior, B. Stevens, R. J. Stouffer, and K. E. Taylor,
668 2016: Overview of the Coupled Model Intercomparison Project Phase 6 (CMIP6) experimental
669 design and organization. *Geoscientific Model Development*, **9 (5)**, 1937–1958, <https://doi.org/10.5194/GMD-9-1937-2016>.

- 674 Farrell, W. E., and J. A. Clark, 1976: On Postglacial Sea Level. *Geophysical Journal International*,
675 **46** (3), 647–667, <https://doi.org/10.1111/J.1365-246X.1976.TB01252.X>.
- 676 Garabato, A. C. N., and Coauthors, 2017: Vigorous lateral export of the meltwater outflow from
677 beneath an Antarctic ice shelf. *Nature*, **542**, 219–222, <https://doi.org/10.1038/nature20825>.
- 678 Golledge, N. R., E. D. Keller, N. Gomez, K. A. Naughten, J. Bernales, L. D. Trusel, and T. L.
679 Edwards, 2019: Global environmental consequences of twenty-first-century ice-sheet melt.
680 *Nature*, **566**, 65–72, <https://doi.org/10.1038/s41586-019-0889-9>.
- 681 Goodman, P. J., 2001: Thermohaline Adjustment and Advection in an OGCM. *Journal of Phys-
682 ical Oceanography*, **31** (6), 1477–1497, [https://doi.org/10.1175/1520-0485\(2001\)031<1477:TAAIA>2.0.CO;2](https://doi.org/10.1175/1520-0485(2001)031<1477:TAAIA>2.0.CO;2).
- 683 Guo, H., Z. Chen, J. Z. Wang, and H. Yang, 2022: Opposite responses of sea level variations to
684 ENSO in the Northwestern Pacific: A transition latitude at 20°N. *Dynamics of Atmospheres and
685 Oceans*, **98**, <https://doi.org/10.1016/J.DYNATMOCE.2022.101288>.
- 686 Hamlington, B. D., and Coauthors, 2020: Understanding of Contemporary Regional Sea-Level
687 Change and the Implications for the Future. *Reviews of Geophysics*, **58** (3), <https://doi.org/10.1029/2019RG000672>.
- 688 Hsieh, W. W., and K. Bryan, 1996: Redistribution of sea level rise associated with enhanced green-
689 house warming: A simple model study. *Climate Dynamics*, **12** (8), 535–544, <https://doi.org/10.1007/BF00207937>.
- 690 Huang, R. X., M. A. Cane, N. Naik, and P. Goodman, 2000: Global adjustment of the thermocline in
691 response to deepwater formation. *Geophysical Research Letters*, **27** (6), 759–762, <https://doi.org/10.1029/1999GL002365>.
- 692 Johnson, H. L., and D. P. Marshall, 2002: A Theory for the Surface Atlantic Response to Ther-
693 mohaline Variability. *Journal of Physical Oceanography*, **32** (4), 1121–1132, [https://doi.org/10.1175/1520-0485\(2002\)032<1121:ATFTSA>2.0.CO;2](https://doi.org/10.1175/1520-0485(2002)032<1121:ATFTSA>2.0.CO;2).
- 694 Johnson, H. L., and D. P. Marshall, 2004: Global Teleconnections of Meridional Overturning
695 Circulation Anomalies. *Journal of Physical Oceanography*, **34** (7), [https://doi.org/10.1175/1520-0485\(2004\)034<1702:GTOMOC>2.0.CO;2](https://doi.org/10.1175/1520-0485(2004)034<1702:GTOMOC>2.0.CO;2).

- 702 Kawase, M., 1987: Establishment of Deep Ocean Circulation Driven by Deep-Water Pro-
703 duction. *Journal of Physical Oceanography*, **17** (12), 2294–2317, [https://doi.org/10.1175/1520-0485\(1987\)017<2294:EODOCD>2.0.CO;2](https://doi.org/10.1175/1520-0485(1987)017<2294:EODOCD>2.0.CO;2).
- 705 Kim, I., D. Hahm, T. S. Rhee, T. W. Kim, C. S. Kim, and S. H. Lee, 2016: The distribution of glacial
706 meltwater in the Amundsen Sea, Antarctica, revealed by dissolved helium and neon. *Journal of*
707 *Geophysical Research: Oceans*, **121** (3), 1654–1666, <https://doi.org/10.1002/2015JC011211>.
- 708 Kopp, R. E., C. C. Hay, C. M. Little, and J. X. Mitrovica, 2015: Geographic Variability of
709 Sea-Level Change. *Current Climate Change Reports*, **1** (3), 192–204, <https://doi.org/10.1007/S40641-015-0015-5/FIGURES/4>.
- 710 Kopp, R. E., J. X. Mitrovica, S. M. Griffies, J. Yin, C. C. Hay, and R. J. Stouffer, 2010: The
711 impact of Greenland melt on local sea levels: A partially coupled analysis of dynamic and static
712 equilibrium effects in idealized water-hosing experiments. *Climatic Change*, **103** (3), 619–625,
713 <https://doi.org/10.1007/S10584-010-9935-1>.
- 714 Lago, V., and M. H. England, 2019: Projected Slowdown of Antarctic Bottom Water Formation
715 in Response to Amplified Meltwater Contributions. *Journal of Climate*, **32** (19), 6319–6335,
716 <https://doi.org/10.1175/JCLI-D-18-0622.1>.
- 717 Li, Q., M. H. England, A. M. Hogg, S. R. Rintoul, and A. K. Morrison, 2023a: Abyssal ocean
718 overturning slowdown and warming driven by Antarctic meltwater. *Nature*, **615**, 841–847,
719 <https://doi.org/10.1038/s41586-023-05762-w>.
- 720 Li, Q., J. Marshall, C. D. Rye, A. Romanou, D. Rind, and M. Kelley, 2023b: Global Climate
721 Impacts of Greenland and Antarctic Meltwater: A Comparative Study. *Journal of Climate*,
722 **36** (11), 3571–3590, <https://doi.org/10.1175/JCLI-D-22-0433.1>.
- 723 Liu, Z., 1999: Planetary wave modes in the thermocline: Non-Doppler-shift mode, advective mode
724 and Green mode. *Quarterly Journal of the Royal Meteorological Society*, **125** (556), 1315–1339,
725 <https://doi.org/10.1002/QJ.1999.49712555611>.
- 726 Lorbacher, K., S. J. Marsland, J. A. Church, S. M. Griffies, and D. Stammer, 2012: Rapid
727 barotropic sea level rise from ice sheet melting. *Journal of Geophysical Research: Oceans*,
728 **117** (C6), <https://doi.org/10.1029/2011JC007733>.

- 730 Lowry, D. P., M. Krapp, N. R. Golledge, and A. Alevropoulos-Borrill, 2021: The influence of emis-
731 sions scenarios on future Antarctic ice loss is unlikely to emerge this century. *Communications*
732 *Earth & Environment*, **2** (1), <https://doi.org/10.1038/s43247-021-00289-2>.
- 733 Marshall, D. P., and H. L. Johnson, 2013: Propagation of Meridional Circulation Anoma-
734 lies along Western and Eastern Boundaries. *Journal of Physical Oceanography*, **43** (12),
735 2699–2717, <https://doi.org/10.1175/JPO-D-13-0134.1>, URL <https://journals.ametsoc.org/view/journals/phoc/43/12/jpo-d-13-0134.1.xml>.
- 736
737 Mitrovica, J. X., C. C. Hay, R. E. Kopp, C. Harig, and K. Latychev, 2018: Quantifying the
738 Sensitivity of Sea Level Change in Coastal Localities to the Geometry of Polar Ice Mass Flux.
739 *Journal of Climate*, **31** (9), 3701–3709, <https://doi.org/10.1175/JCLI-D-17-0465.1>.
- 740 Moorman, R., A. K. Morrison, and A. M. Hogg, 2020: Thermal Responses to Antarctic Ice Shelf
741 Melt in an Eddy-Rich Global Ocean–Sea Ice Model. *Journal of Climate*, **33** (15), 6599–6620,
742 <https://doi.org/10.1175/JCLI-D-19-0846.1>.
- 743 Morlighem, M., and Coauthors, 2020: Deep glacial troughs and stabilizing ridges unveiled beneath
744 the margins of the Antarctic ice sheet. *Nature Geoscience*, **13** (2), 132–137, <https://doi.org/10.1038/s41561-019-0510-8>.
- 745
746 Nieves, D., and M. Spall, 2018: Propagation of North Atlantic Deep Water Anomalies. *Journal of*
747 *Physical Oceanography*, **48** (8), 1831–1848, <https://doi.org/10.1175/JPO-D-18-0068.1>.
- 748 Oppenheimer, M., and Coauthors, 2019: Sea Level Rise and Implications for Low-Lying Islands,
749 Coasts and Communities. *IPCC Special Report on the Ocean and Cryosphere in a Changing*
750 *Climate*, H.-O. Pörtner, D. C. Roberts, V. Masson-Delmotte, P. Zhai, M. Tignor, E. Poloczanska,
751 K. Mintenbeck, A. Alegría, M. Nicolai, A. Okem, J. Petzold, B. Rama, and N. M. Weyer, Eds.,
752 Cambridge University Press, 321–445, <https://doi.org/10.1017/9781009157964.006>.
- 753 Otosaka, I. N., and Coauthors, 2023: Mass balance of the Greenland and Antarctic ice sheets
754 from 1992 to 2020. *Earth System Science Data*, **15** (4), 1597–1616, <https://doi.org/10.5194/ESSD-15-1597-2023>.

- 756 Park, J. Y., F. Schloesser, A. Timmermann, D. Choudhury, J. Y. Lee, and A. B. Nellikkattil,
757 2023: Future sea-level projections with a coupled atmosphere-ocean-ice-sheet model. *Nature*
758 *Communications*, **14**, <https://doi.org/10.1038/s41467-023-36051-9>.
- 761 Pedlosky, J., 1965: A note on the western intensification of the oceanic circulation. *Journal*
760 *of Marine Research*, **23** (3), URL https://elischolar.library.yale.edu/journal_of_marine_research/
761 1055.
- 764 Penn, J., and G. K. Vallis, 2018: Linear Shallow Water Model. URL <https://empslocal.ex.ac.uk/people/staff/gv219/codes/linearslallowwater.py>.
- 765 Pritchard, H. D., S. R. M. Ligtenberg, H. A. Fricker, D. G. Vaughan, M. R. Van Den Broeke, and
766 L. Padman, 2012: Antarctic ice-sheet loss driven by basal melting of ice shelves. *Nature*, **484**,
766 502–505, <https://doi.org/10.1038/nature10968>.
- 767 Rignot, E., S. Jacobs, J. Mouginot, and B. Scheuchl, 2013: Ice-shelf melting around Antarctica.
768 *Science*, **341** (6143), 266–270, <https://doi.org/10.1126/science.1235798>.
- 769 Schmidt, G. A., and Coauthors, 2023: Anomalous Meltwater From Ice Sheets and Ice
770 Shelves Is a Historical Forcing. *Geophysical Research Letters*, **50** (24), <https://doi.org/10.1029/2023GL106530>.
- 772 Smith, R. S., and Coauthors, 2021: Coupling the U.K. Earth System Model to Dynamic Models
773 of the Greenland and Antarctic Ice Sheets. *Journal of Advances in Modeling Earth Systems*,
774 **13** (10), <https://doi.org/10.1029/2021MS002520>.
- 775 Stammer, D., 2008: Response of the global ocean to Greenland and Antarctic ice melting. *Journal*
776 *of Geophysical Research: Oceans*, **113** (C6), <https://doi.org/10.1029/2006JC004079>.
- 777 Sun, S., A. F. Thompson, and I. Eisenman, 2020: Transient Overturning Compensation be-
778 tween Atlantic and Indo-Pacific Basins. *Journal of Physical Oceanography*, **50** (8), 2151–2172,
779 <https://doi.org/10.1175/JPO-D-20-0060.1>.
- 780 Swart, N. C., and Coauthors, 2023: The Southern Ocean Freshwater Input from Antarctica (SOFIA)
781 Initiative: scientific objectives and experimental design. *Geoscientific Model Development*,
782 **16** (24), 7289–7309, <https://doi.org/10.5194/gmd-16-7289-2023>.

- 783 Taylor, K. E., R. J. Stouffer, and G. A. Meehl, 2012: An Overview of CMIP5 and the Experiment
784 Design. *Bulletin of the American Meteorological Society*, **93** (4), 485–498, <https://doi.org/10.1175/BAMS-D-11-00094.1>.
- 786 Todd, A., and Coauthors, 2020: Ocean-Only FAFMIP: Understanding Regional Patterns of Ocean
787 Heat Content and Dynamic Sea Level Change. *Journal of Advances in Modeling Earth Systems*,
788 **12** (8), <https://doi.org/10.1029/2019MS002027>.
- 789 Vandermeirsch, F. O., X. J. Carton, and Y. G. Morel, 2003: Interaction between an eddy and a
790 zonal jet: Part II. Two-and-a-half-layer model. *Dynamics of Atmospheres and Oceans*, **36** (4),
791 271–296, [https://doi.org/10.1016/S0377-0265\(02\)00066-0](https://doi.org/10.1016/S0377-0265(02)00066-0).
- 792 Zhai, X., H. L. Johnson, and D. P. Marshall, 2011: A model of Atlantic heat content and sea
793 level change in response to thermohaline forcing. *Journal of Climate*, **24** (21), 5619–5632,
794 <https://doi.org/10.1175/JCLI-D-10-05007.1>.
- 795 Zhai, X., H. L. Johnson, and D. P. Marshall, 2014: A Simple Model of the Response of the Atlantic
796 to the North Atlantic Oscillation. *Journal of Climate*, **27** (11), 4052–4069, <https://doi.org/10.1175/JCLI-D-13-00330.1>.